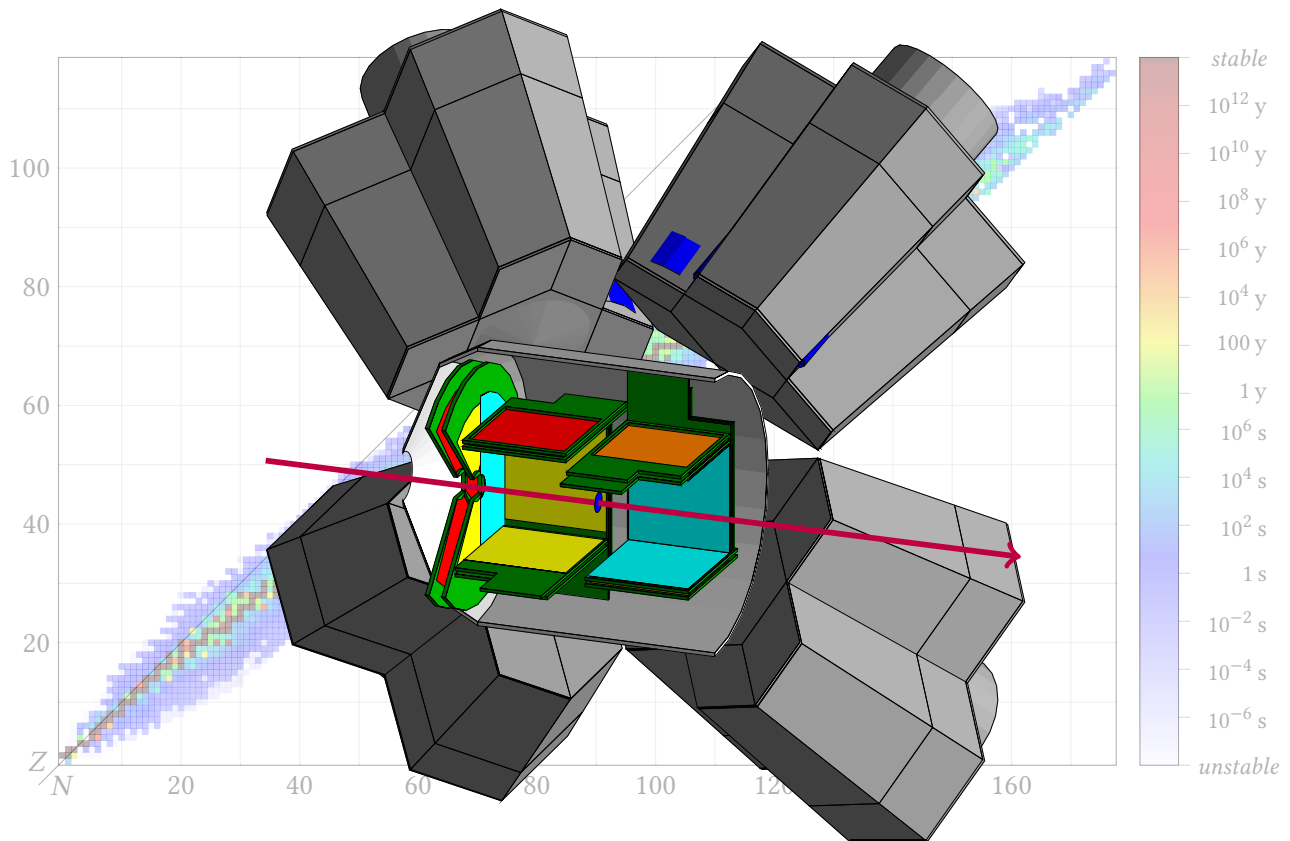




CHALMERS



Neutron detection with the MINIBALL germanium array

Master's thesis in Fundamental physics

DANIEL ANDERSSON

MASTER'S THESIS IN FUNDAMENTAL PHYSICS

Neutron detection with the MINIBALL germanium array

DANIEL ANDERSSON

Department of Fundamental physics
Division of Subatomic physics
CHALMERS UNIVERSITY OF TECHNOLOGY
Göteborg, Sweden 2015

Neutron detection with the MINIBALL germanium array
DANIEL ANDERSSON

© DANIEL ANDERSSON, 2015

ISSN 1652-8557
Department of Fundamental physics
Division of Subatomic physics
Chalmers University of Technology
SE-412 96 Göteborg
Sweden
Telephone: +46 (0)31-772 1000

Cover:
Cutaway rendering of the T-REX and MINIBALL setup at REX-ISOLDE (see Section 3.2)
on top of a graph of the known isotopes and their half-lives.

Chalmers Reproservice
Göteborg, Sweden 2015

Neutron detection with the MINIBALL germanium array
Master's thesis in Fundamental physics
DANIEL ANDERSSON
Department of Fundamental physics
Division of Subatomic physics
Chalmers University of Technology

ABSTRACT

In experiment Is430 at REX-ISOLDE, CERN, transfer reactions of neutron-rich beryllium isotopes on deuterated targets were studied with the segmented germanium detector array MINIBALL, detecting electromagnetic radiation, and the silicon-based T-REX detector for charged particles. This thesis investigates signals in MINIBALL following inelastic scattering of neutrons on ^{72}Ge , populating its first excited state which decays through ejecting a monoenergetic electron — a technique to detect neutrons in germanium detectors based on a proof-of-concept article.

By correlating these neutron signals with additional event information, there is a possibility to draw a more complete picture of the reactions involved without the need to add additional detection equipment. Monitoring of these events could also have possible uses in online analysis of the neutron rate hitting the detectors, possibly degrading their function.

This work investigates to which extent this process can be of help in the T-REX and MINIBALL configuration at ISOLDE in particular, and for germanium detectors in general.

Keywords: Neutron detection, REX-ISOLDE, Transfer reactions, Exotic nuclei, Semiconductor detectors

SAMMANFATTNING

I experiment Is430 vid REX-ISOLDE, CERN, studerades transferreaktioner med neutronrika isotoper av beryllium mot ett deuteriummål med hjälp av den segmenterade germanium-detektorn MINIBALL för elektromagnetisk strålning samt den kiselbaserade T-REX-detektorn för laddade partiklar. Denna uppsats undersöker signaler i MINIBALL som härrör från inelastisk spridning av neutroner mot ^{72}Ge , vilket populerar isotopens första exciterade tillstånd som i sin tur deexciteras genom att sända ut en elektron med en känd energi – en teknik för att detektera neutroner i germaniumdetektorer som beskrivits i tidigare artiklar.

Genom att korrelera dessa neutrons signaler med ytterligare observabler så finns det möjlighet att måla upp en mer komplett bild av en reaktion utan att behöva installera ytterligare detektorutrustning. Övervakning av dessa signaler skulle också kunna komma till nytta för att illustrera neutronflödet mot detektorn, vilket är en process som potentiellt kan försämra en sådan detektors funktion.

Denna uppsats undersöker till vilken grad analys av denna process kan vara till nytta för T-REX- och MINIBALL-konfigurationen vid ISOLDE i synnerhet, och för germaniumdetektorer i allmänhet.

PREFACE

This thesis concludes my education for the degree of “Civilingenjör i Teknisk fysik” (translated to “Master of Science in Engineering physics”) from Chalmers University of Technology, consisting of a BSc in “Engineering physics”, an MSc in “Fundamental physics” and the obligatory additional courses required at Chalmers for the degree of “Civilingenjör” in this particular discipline.

The text is written for a reader with a physics background equivalent to a bachelor’s degree or above, with the added intention that at least the introductory chapter should be possible to digest for a general audience. If not, feel free to ask me questions.

ACKNOWLEDGEMENTS

My time in the subatomic physics group and the subatomic world in general has been nothing but pleasant and instructive, both in nuclear and common matters, and there are several individuals who I have to thank for making it so.

The pragmatic guidance from Professor Thomas Nilsson was probably a prerequisite for me finishing the project, as time kept on passing. I have also had the pleasure to take the introductory bachelor’s level “Subatomär fysik” course, as well as the master’s level “Advanced subatomic physics” (where a guest lecture by Thomas was what made me attend the next course mentioned) and “Modern subatomic detection and analysis methods” (which quite directly led to this thesis) courses under his lecturing, which have all given me new insights on physics and the world around us. As part of the latter courses and this particular project, I have also gotten to accompany him in trains and planes to both CERN and GSI to experience actual experimental facilities for subatomic physics research, which certainly are experiences I will remember and cherish for life. Last but not least he has repeatedly invited me to eat “smörgåstårta” on the VIP plateau during the lunch break at the yearly “Vetenskapsfestivalen”^{*} in Gothenburg – students always appreciate food!

The quality of both the information and the language in this thesis depends to a large part on the continuous feedback from Associate Professor Andreas Heinz, both in written and verbal form. I believe I have still not had a conversation with Andreas where I felt that I did not learn anything new. His physics experience and ability to never seem to be far away from a laugh is certainly an asset in the group, and his attention to detail has been much appreciated.

To account for all interactions within the group I would have to carry on for several pages, which I will avoid, but some additional specific individuals I want to mention include Håkan Johansson, with whom I have had several late evening talks about highly

^{*}“The International Science Festival”; <http://vetenskapsfestivalen.se/>.

interesting technical subjects that would probably bring the majority of the population to swift sleep (Linux, Debian, drive reliability, ASICs, Git, Bitcoin, ...still awake?). I also remember discussions on similar topics with Hans Törnqvist as I met him in the ISOLDE hall at CERN, where he immediately showed his prowess with GDB to make the analysis code run on the local machines, and with Rikard Lundmark who shared my office and gripes with the ROOT data analysis framework. I would also like to mention Professor Emeritus Björn Jonson whom I have met several times during the project, both at group meetings at Chalmers and in the vicinity of the ISOLDE hall and during lunchtimes at CERN, who always has stories to tell. I also highly appreciated the interest shown for my project by Professor Emeritus Göran Nyman, and the talks we had about, among other things, careers in the field of subatomic physics on our walk to a joint division dinner in central Gothenburg.

During my short stay at Aarhus University, I was well taken care of by the group. I can particularly mention Jacob Johansen who introduced me to the code suite used for the experiment analysis, and even had the courage and good judgement to lend me lunch money at CERN (which was returned when he visited our group at Chalmers, I promise). During the experiment itself, Associate Professor Karsten Riisager put faith in me and PhD student Gunvor Koldste to perform almost-online analysis of the experimental data to present histograms at the daily group meetings at ISOLDE, which was much more interesting than just sitting around watching the equipment and others working, which was my initial realistic expectation of my presence during the experiment. It is always nice when the hours and years of spare time spent in front of terminal windows come to use.

I would like to thank Kathrin Wimmer for giving me permission to use a figure from her PhD thesis. Speaking of the German collaboration partners from Munich, I also enjoyed spending time with both Vinzenz Bildstein and Dennis Mücher who constituted the main detector expertise during the experiment run, and also knew a thing or two about German participants in the Eurovision Song Contest.

On a more technical note, I was grateful for the \LaTeX thesis template shared by Mikael Öhman which provided a layout framework for this very thesis,^{*} upon the foundation of which I had the joy of fiddling with parameters and layouts for many, many hours.[†] I would also like to thank Christian Feuersänger who created the PGFPlots package which was used for graph creation in this thesis, and also provided direct support when I began

^{*}The fact that Chalmers itself does not provide such templates in a centralised manner when a majority of students in at least select institutions choose this method is frankly surprising — not least since my understanding is that \LaTeX is also more or less a requirement for journal publications.

[†]In the words of Richard Feynman from *Surely you're joking, Mr. Feynman!* (1985): “The trouble with computers is you *play* with them.”

to push the limits of the package.*

On a less technical and more personal note, I am assured (at least certainly hope) that my fiancée Johanna knows how much she means to me, not only with regards to pushing through and actually finishing this thesis and getting my degree, but in my life in general.

*<http://tex.stackexchange.com/q/180648>

This page intentionally contains only this sentence.

NOMENCLATURE AND CONVENTIONS

Masses in particle physics are in general expressed in the energy unit electron volts (eV), where 1 eV corresponds to the amount of energy an electron gains (or loses) when moved across an electric potential difference of 1 V. This practice is coupled to another common convention in the field: the use of *natural units*, where certain fundamental constants of nature are set to 1, i.e. dimensionless unity. With this simplifying notation for c , the speed of light in vacuum, Einstein’s mass-energy equivalence formula for a particle at rest takes the appealing form $E = m$, which shows the motivation for using an energy unit such as electron volts as a direct measure of mass.

Transforming back to “regular” units becomes a case of balancing the dimensions by factors of the fundamental constants and inserting needed numeric scaling factors. As an example, going from a mass expressed in electron volts in natural units to kilograms in SI units can be done by converting the electron volt quantity to SI units by expressing the elementary charge e in coulombs and balancing units to retrieve an SI mass unit:

$$\begin{aligned} 1 \text{ eV} &= 1.602 \cdot 10^{-19} \text{ C V} \\ &= 1.602 \cdot 10^{-19} \cancel{\text{A s}} \cdot \text{W}/\cancel{\text{A}} \\ &= 1.602 \cdot 10^{-19} \text{ J} \\ &= 1.602 \cdot 10^{-19} \text{ kg m}^2/\text{s}^2. \end{aligned}$$

By dividing with a velocity squared, specifically c^2 (exactly the factor that was omitted from the mass-energy equivalence relation to begin with), another scaling factor is added and the units will yield a “proper” SI mass.

In a similar way, momentum \vec{p} with magnitude p can be expressed in electron volts (or eV/c without natural units), which is motivated by comparison with the expression for total relativistic energy:

$$E^2 = p^2 + m^2.$$

For a massless particle, we directly reach $E = p$, which is subject of a rationale similar to the one shown above for the rest mass.

Benefits include quick answers to questions like: “What energy will a helium nucleus accelerated across an electric potential of 3 MV gain?” — taking the charge ($+2e$) times the potential directly yields 6 MeV; “Which particles can be produced in a collision with 3 GeV available centre-of-mass energy?” — well, certainly not more than what combines for a rest mass of 3 GeV.*

*“At least not for prolonged times”, adds Heisenberg.

This page intentionally contains only this sentence.

CONTENTS

Abstract	iii
Sammanfattning	iv
Preface	v
Acknowledgements	v
Nomenclature and conventions	ix
Contents	xi
1 Introduction	1
1.1 Project chronology	2
1.2 Why study neutron-rich beryllium isotopes?	2
1.2.1 The shell model and complications	3
1.2.2 The unusual properties of neutron-rich beryllium isotopes	5
1.3 Particle physics at CERN	6
1.3.1 The ISOLDE facility	9
1.4 Subatomic physics at Chalmers	9
2 Background	11
2.1 Nuclear states	11
2.1.1 Transitions and selection rules	12
2.2 Nomenclature of nuclear reactions	13
2.2.1 Transfer reactions	14
2.2.2 Compound reactions	14
2.3 Nuclear reaction kinematics	15
2.4 Detection principles	16
2.4.1 Charged particles	17
2.4.2 γ rays	18
2.4.3 Neutrons	19
2.5 Beryllium	21
2.6 Beam delivery	22
2.6.1 Proton acceleration	22

2.6.2	The ISOLDE facility	23
2.6.3	REX-ISOLDE	23
2.7	Semiconductor detectors	25
2.7.1	Materials used	26
2.7.2	Position detection for charged particles with DSSTDs	27
2.7.3	Particle identification	27
3	Experiment	29
3.1	Run configuration	29
3.1.1	Beam	29
3.1.2	Targets and sources	30
3.1.3	Runs	31
3.2	Detectors	31
3.2.1	MINIBALL	31
3.2.2	T-REX	31
3.3	Detector calibration	33
3.3.1	MINIBALL	33
3.3.2	T-REX	34
3.4	Data capture and processing	34
3.4.1	Relevant available observables	35
3.4.2	Analysis assumptions	36
4	Results and analysis	37
4.1	Improving signal-to-noise ratio	37
4.1.1	Backward versus forward angles	37
4.1.2	Event timing considerations	37
4.2	Coincidence measurements	42
4.2.1	Neutron and γ coincidences from the (d,n) reaction	42
4.2.2	Neutron and ion coincidences from the (d,n) reaction	42
5	Summary	49
5.1	Conclusions	49
5.2	Outlook	50
	References	54

A	Appendix	61
A.1	Code samples	61
A.1.1	Intermediate tree creation	61
A.1.2	Histogram creation with Python	70
A.1.3	Kinematic curve with MATLAB	74

This page intentionally contains only this sentence.

1

Introduction

The stability of the elements that constitute the matter around us is studied in nuclear physics. Knowledge of the extent to which certain configurations of particles will transmute into other configurations, emit radiation or stay stable has uses within human safety regulations, the medical sciences, energy production and even more areas of direct human interest. In addition, the discoveries within nuclear physics have helped to produce theories concerning the fundamental physical laws that govern our existence.

One approach to investigate the subatomic world of the nucleus is to study collisions between nuclei. The observable effects are recorded through detectors and analysed with methods that are continuously improved upon by scientists all over the world. Such an experiment involves steps such as isotope production, particle acceleration, particle and radiation detection, data recording and analysis, all of which bring their own engineering challenges.

A particular aspect overarching the experiment studied in this thesis is the production and acceleration of exotic radioactive beams to bring insights on isotopes normally not found in nature – insights which in turn can be helpful when formulating general theories on the composition and stability of nuclei.

Electromagnetically charged particles are well suited for the electronic equipment that for several reasons is preferred to use to detect events, in that these particles directly can trigger a measurable current of electrons in the detectors. Though still subject of several complications regarding energy ranges and event rates, charged particles are substantially easier to detect than electrically neutral particles such as the neutron.

The motivation behind the project described in this thesis is to investigate a method to detect neutrons via secondary effects in a semiconducting detector present for another primary task in experiment Is430 at ISOLDE, CERN. Such a method could potentially be of help in reconstructing nuclear events from experiment data or for diagnostic purposes, without having to install additional detection equipment.

This introductory chapter contains a more elaborate historical background on some

of the challenges in nuclear physics, followed in the next chapter by a brief description of the theoretical framework underlying the experiment. The experiment conditions are accounted for in the third chapter, the plots produced by my part of the project together with an analysis in the fourth, finishing with conclusions and an experimental outlook in chapter five.

1.1 Project chronology

As part of my thesis I took part in experiment Is430: “Study of neutron-rich Be isotopes with REX-ISOLDE”, which took place at CERN in the ISOLDE hall in September 2010. Professor Thomas Nilsson* and Associate Professor Karsten Riisager† showed me proof-of-concept articles concerning a technique to identify neutrons in germanium detectors [1, 2] and suggested that I should perform a similar analysis of the data from the experiment. The initial goal was to study to what extent this approach could help to distinguish between certain reaction channels that could not be uniquely identified through other methods, and explore if there was even more information to be found using this approach.

By finding characteristic secondary excitations of certain germanium isotopes in the MINIBALL detector resulting from neutron impact, the existence of neutrons from the transfer reactions can be deduced. The data analysis performed in this paper concerns identification of these signals, finding ways to improve the signal-to-background ratio and to connect the detected signals to actual physical phenomena.

I visited Riisager’s group at Aarhus University in early September 2010, where I was introduced to the computational tools and experimental history of Is430 to a large part by then PhD student Jacob Johansen. I later participated in the experiment at CERN together with those already mentioned as well as other scientists, including Chalmers-based then PhD student Hans Törnqvist, at the time situated at CERN, and people from TUM‡ in Munich and IEM§ in Madrid.

After a longer intermission following the experiment, my work was resumed in September 2013. By this time Johansen had done some preliminary analysis of the neutron detection in his PhD thesis. First indications pointed towards too low statistics for useful results in coincidence with the charged particle events that were the main interest of Johansen, but the analysis was far from complete, and it was suggested by Nilsson and Riisager that I could continue this work, which is the subject of the following thesis.

1.2 Why study neutron-rich beryllium isotopes?

A starting point for nuclear physics were the scattering experiments of Rutherford in 1911, just over 100 years ago, which for the first time showed the existence of an actual atomic

*Chalmers University of Technology.

†Aarhus University.

‡Technische Universität München.

§Instituto de Estructura de la Materia.

nucleus. This was followed by a period of intense theoretical advancements, kick-starting quantum mechanics and particle research. In the century that followed, nuclear science in the eyes of the general society was subject of intensive research with large geopolitical implications concerning subjects such as warfare, growing energy needs and sustainability, but it was also used as a tool to probe into theories on the origins of the universe, medical research and material advancement, just to mention a few key topics.

With all this interest and funds invested over a century: how come research is not “done”, and why should rough treatment of an unusual isotope of beryllium be of any help in gaining further knowledge?

1.2.1 The shell model and complications

In nuclear physics, the nuclear *shell model* [3], which led to the Nobel prize in physics in 1963 being awarded to Goeppert-Mayer, Jensen and Wigner [4], is an analogue to the perhaps better known atomic shell model, where electrons are modelled to be situated in shells based on the Pauli exclusion principle.* In atomic theory, electron shells that are “filled”, i.e. have electrons occupying each possible quantum number combination in the specific shell, are the most energetically favourable configurations and therefore the most stable. Filled shells are in fact stable enough to let atomic properties to a large degree be based solely on the electrons not bound in these filled shells – so called “valence electrons”. This phenomenon is the basis for the power of the periodic table of elements, where the element columns have similar valence configurations and thus similar chemical properties.

When nuclear science began to investigate the *separation energy*[†] for protons and neutrons (collectively known as *nucleons*) for different nuclei, a pattern emerged where a higher number of protons, Z , and number of neutrons, N , as a tendency made this energy increase[‡] except at a few key values after which it dropped notably – values known as *magic numbers*.[§] This pattern resembled how atomic properties varied smoothly with an increased number of electrons, with drastic changes generally occurring at filled electron shells, which sparked hope of finding a similar model for the nucleus. How such a model could be formed, despite the apparent differences in the underlying mechanisms, occupied nuclear scientists during the late first half of the 20th century.

One issue when building such a nuclear model is the nature of the potential in which the constituents reside. In atomic physics, the electromagnetic potential of the nucleon that is felt by the orbiting electron can, for most intents and purposes, be assumed to arise from a perfectly stationary nucleus during the interaction of the electron. This is due to the electron mass being much smaller than the mass of a nucleon, by a factor of nearly two-thousand, in analogy to how we often safely assume that the Sun is stationary at the centre of mass of our solar system in related calculations. In nuclear physics, however, the luxury of assuming a central potential is not available since the forces affecting a certain nucleon

*The principle states that two identical fermions (half-integer intrinsic spin particles) cannot occupy the same quantum state simultaneously.

[†]The energy needed to remove the particle from the nucleus.

[‡]Actually with a minor “sawtooth pattern” due to the nucleon pairing effect.

[§]2, 8, 20, 28, 50, 82, 126 – the continuation of this series is subject to research.

originate from other *similar* nucleons, and the dynamics of a single nucleon therefore to a large extent couples to the movements of the others, which in turn influences the original nucleon.

Another complicating aspect is the properties of the forces involved: where atomic physics needs almost exclusively only worry about the well understood electromagnetic interaction, the nucleons interact to a large degree as a consequence of the *strong nuclear force*. The strong force governs the interaction between the quarks and gluons: the constituents of the nucleons. This complicated interplay within the nucleons impact the nucleon–nucleon interactions via the *residual strong force*, i.e. secondary effects of an internal structure which adheres to rules that are not fully understood. Calculations of these forces are severely limited by their complexity, and simplifying assumptions are essential in reaching results. In contrast, the simplest atomic systems even permit themselves to complete analytical closed form solutions, forming a basis for solutions of more advanced systems by viewing complicating additions as small *perturbations* from the solved models. It is not the intention to call atomic physics “easy”, and more precise calculations certainly bring countless subtleties, but the range over which successful predictions of energy levels are possible is large in comparison with studies of nuclei.

Despite these (and more) complications, viewing nuclei in terms of closed shells of protons and neutrons and “left-over” *valence nucleons* that to a large degree are responsible for the behaviour of the nucleus has been a fruitful model. The magic numbers are commonly used to explain the stability of certain isotopes and the decay chains of others.

The predictions of the nuclear shell model are generally successful for the stable isotopes in the “central lane” – known as the *valley of stability* – of a nuclear chart of observed isotopes (see Figure 1.1). As we move toward the neutron and proton excessive edges of the chart, the stability diminishes as we approach the theoretical limits where nuclei no longer bind, known as the *drip lines*. These isotopes are not found naturally,* but can be explored with the advent of particle accelerators able to create these *exotic nuclei*.

*If they initially were here, they would have already decayed and thus been gone.

Experiments have explored the proton-rich drip line up to protactinium at $Z = 91$, but the neutron line has only been followed up to oxygen at $Z = 8$ [5]. At the relatively unexplored neutron-rich side, experiments discovered a region of isotopes whose properties strayed from the magic numbers predicted by the shell model [6, 7]. This region was named the *island of inversion*, and subsequently even more such “islands” were found. The lightest such region occurs along the $N = 8$ line, centred on ^{11}Li and including ^{12}Be [8, 9], which is reachable from the beam in Is430. Since the isotopes in this region pose challenges to existing nuclear models, they are of large interest to study in order to find how these models need to be modified to correctly account for the configurations that are available and their respective properties. Better models will in turn allow more successful *predictions* of properties without having to perform extensive (and expensive) experiments for every

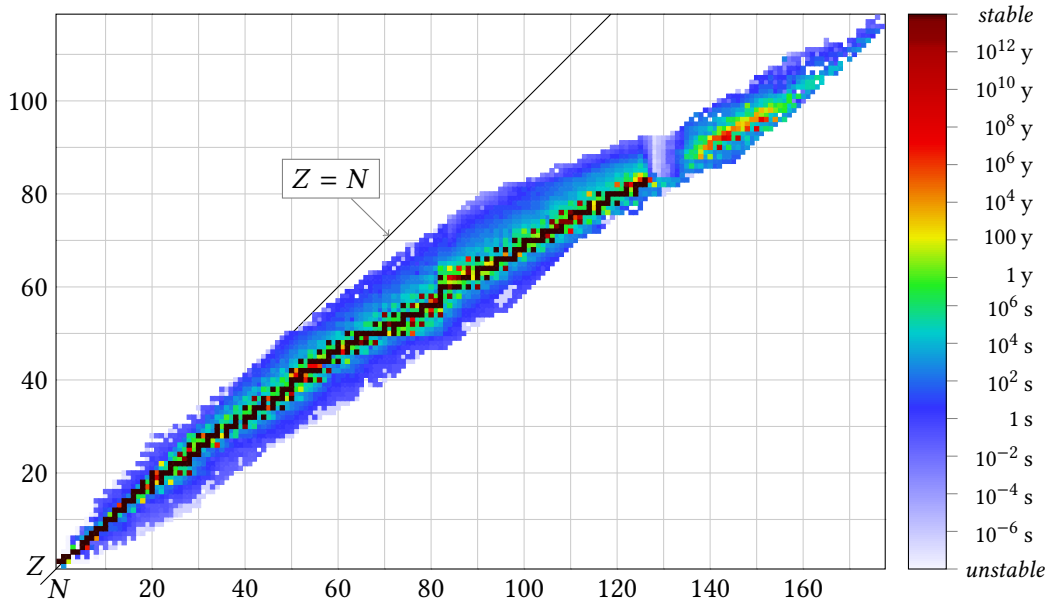


FIGURE 1.1: A table of known isotopes with colour-coded half-lives (isotope data from Brookhaven National Laboratory [10]). Z denotes the number of protons and N the number of neutrons.

possible configuration.

Why not just find a general formula and calculate all these numbers from first principles? A complete and practically usable so-called *ab initio* approach might be the dream, finally answering all questions on isotope stability and other properties, but nature has not produced a simple phenomenon to work with, which has hopefully been hinted in this section. Without digging too deep into nuclear potential theory, we can appreciate the need for experiments to guide improved empirical models.

1.2.2 The unusual properties of neutron-rich beryllium isotopes

One of the needed simplifying assumptions in nuclear calculations is based on the tendency of nature to prefer certain nucleon *clusters* over others, e.g. the α particle consisting of two protons and two neutrons (also known as the nucleus of the by far most prevalent helium isotope, ${}^4\text{He}$). Its high binding energy leads to a “clumping” of nucleons *within* nuclei to α clusters where possible.

This effect has profound influence on and can be viewed as the origin of α decay. By modelling the inner workings of a nucleus as containing preformed α particles and calculating the probability of such an α tunneling out of the nuclear potential well, Gamow constructed in 1928 a successful theoretical model able to predict the activity of α -decaying

nuclei [3].

In a similar vein, a nucleus of four protons and four neutrons can for calculational purposes be simplified by viewing it as system of two closely bound α particles. Instead of eight bodies, we now only need to focus on two, where the assumption lies in that the two α nuclei will stay bound and not let their respective constituents freely interact. That particular case would describe ${}^8\text{Be}$ as 2α , and insights on other so called $N\alpha$ nuclei, consisting of a multiple N of α constituents,* can arise from this viewpoint [11, 12, 13].

* ${}^4\text{He}$, ${}^8\text{Be}$, ${}^{12}\text{C}$, etc.

In a close extension of this model, adding a neutron, n , to the very loosely bound (due to the constituent α particles tight respective internal bonds) ${}^8\text{Be}$ to create ${}^9\text{Be}$ exhibits behaviour of a $2\alpha + n$ nucleus, with an image of the lone neutron acting as the “glue” (analogous to the atomic notion of a covalent bond) that keeps the α particles together, resulting in the only stable isotope of beryllium [14]. The addition of yet another neutron yields a similar structure in the long-lived ${}^{10}\text{Be}$ isotope.

Continuing the chain to ${}^{11}\text{Be}$ — the isotope produced for this experiment — will keep the basic structure of ${}^{10}\text{Be}$, where the extra neutron will be very weakly bound with a position distribution extending far beyond the traditional view of a nucleus, tunnelling out into the *classically forbidden region*. The general descriptive term for such systems, where one or several nucleons can be found far from the typical radius of a nucleus, is *halo nuclei* [15]. The clustering in ${}^{11}\text{Be}$ can be described as $2\alpha + 2n + n$ (see Figure 1.2) [16]. The unpaired neutron will extend far from the core nucleus, and its separation energy is low.

Being a halo nucleus, relating to isotopes of disappearing magic numbers as mentioned in Section 1.2.1 and being difficult to model by existing methods (though still within range of computational limits) are reasons all adding to the motivation of studying ${}^{11}\text{Be}$.

1.3 Particle physics at CERN

The largest particle physics laboratory in the world is run by the research organisation CERN,[†] which along with its main facilities is based on the Franco-Swiss border outside of Geneva. From its establishment by 12 states in 1954, the organisation has grown to 21 full member states, 20 of which are European [17]. In addition, several non-European entities have observer status and other roles within the project, today making it a truly global endeavour.

Sweden was one of the founding states and its involvement continues to this day. It is represented in place by research groups from the Royal Institute of Technology, Stockholm University, Uppsala University, Lund University and Chalmers University of Technology [19], and contributes yearly funding via the Swedish Research Council, which in 2014 equalled 29 million Swiss francs[‡] of CERN’s total yearly budget of 1.1 billion Swiss francs [20].

[†]Officially *Organisation Européenne pour la Recherche Nucléaire*, i.e. the “European organisation for nuclear research”, though commonly known through its historical acronym CERN.

[‡]As of writing in 2014, 1 CHF \approx 7.6 SEK \approx 0.8 €.

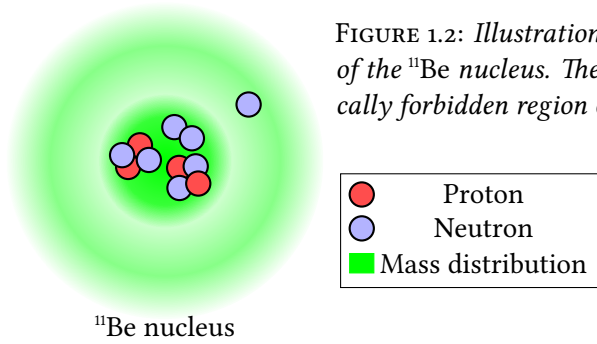


FIGURE 1.2: *Illustration of the $2\alpha + 2n + n$ type halo structure of the ^{11}Be nucleus. The stray neutron can move in the classically forbidden region outside of the strong potential barrier.*

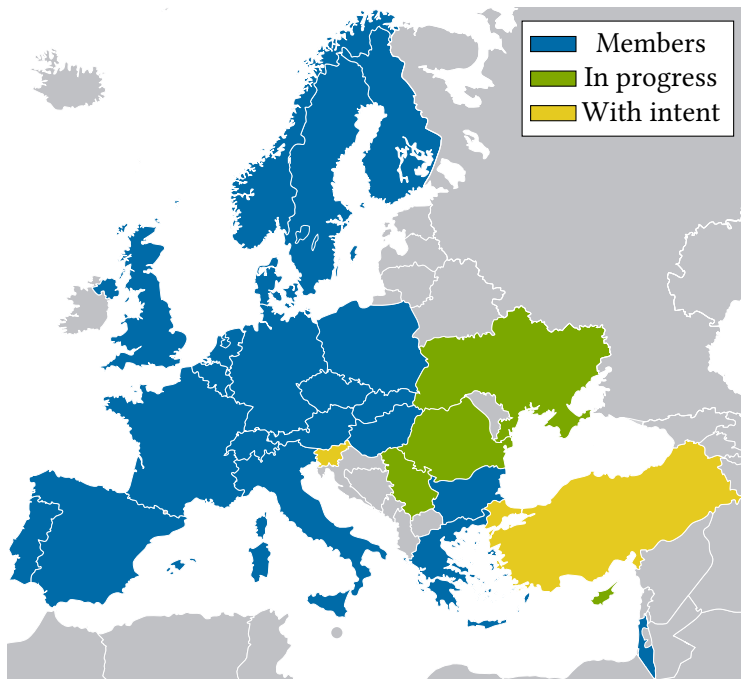


FIGURE 1.3: *Map of CERN members, states in progress of becoming members and states that have declared intentions of joining the organisation as of 2014 [17, 18].*

CERN provides large research facilities for which collaborators can apply for usage. After evaluating scientific merit and feasibility, a time schedule is decided with slots portioned out to different projects.

Mentioning all significant scientific achievements of CERN would constitute a thesis in itself, but historical highlights include:

Muon research. The “ $g-2$ ” experiment, which began in 1959 and published its final results in 1979, investigated a dimensionless quantity g relating the magnetic dipole moment and the intrinsic angular momentum of the muon [21]. The experiment name refers to the prediction of Dirac theory which yields $g = 2$, identically, but previous experimental results for the electron, a sister particle of the muon, consistently showed a slightly higher value. The long running muon experiment at CERN gave the most precisely measured values of this type for its time, triggering further calculations and developments of quantum electrodynamics.

Carriers of the weak force. After first noticing traces of a neutral current carrier in a bubble chamber at CERN in 1973, both the W^\pm and Z^0 bosons, theorised to be the carriers of the weak force,* could be unambiguously detected ten years later with the help of the *Super Proton Synchrotron* (SPS) [22, 23]. This promptly awarded the first Nobel prize directly related to CERN’s activities to Carlo Rubbia and Simon van der Meer in 1984 [24], in what has been described as a defining moment in shifting the power balance in particle physics back towards Europe from American dominance since the second world war [25].

*An interaction between fermions responsible for among other things radioactive decay.

Quark-gluon plasma. The SPS experiments with heavy lead ions that started in 1994 reached previously unavailable high temperatures and pressures of nuclear matter. This produced the first experimental signs of a new state of matter named *quark-gluon plasma* (QGP) which were announced in early 2000 [26]. In this state, which is believed to have been present a couple of microseconds after the big bang, the energy density is sufficiently high for the hadronic[†] constituents of quarks and gluons to form a plasma. Following the primary announcement from CERN, further experiments continued exploring QGP, both in the USA and the subsequent *Large Hadron Collider* (LHC) at CERN itself [27].

[†]“Hadron” is a collective term for strongly interacting particles, including e.g. protons and neutrons.

The Higgs boson. The hunt for the observation of the final missing particle in the *standard model*[‡] ended in 2012 after two independent teams working at the LHC collaboratively announced detection of a new particle with Higgs-like properties at a certain energy [28]. Further analysis confirms this initial statement [29], and it quickly rendered the Nobel prize in physics 2013 to Peter Higgs and François Englert who had participated in postulating the particle some 50 years earlier [30].

[‡]A highly successful theory describing the electroweak and strong interactions of subatomic particles.

1.3.1 The ISOLDE facility

Operating since 1967, ISOLDE is currently the longest running experiment at CERN [31, 32]. Studying radioactive nuclides in low-energy experiments, it has provided the scientific community with extensions of and insights into the nuclear chart, enhancements of isotope mass measurements and much more. Recently celebrating its 50 year anniversary as an active project, it is kept relevant through a series of equipment and technique upgrades – see Section 2.6.2 for more details.

1.4 Subatomic physics at Chalmers

The *Subatomic physics division* organised under the *Department of Fundamental Physics* at Chalmers University of Technology today performs both experimental and theoretical work in nuclear physics [33]. The experimental branch, within which this thesis project was carried out, is active both at GSI,* where it is directly involved in current experiments, at CERN, where it performs experiments at the ISOLDE facility as part of the MAGISOL collaboration which also includes groups at Aarhus University and IEM in Madrid, and with the development of the new FAIR[†] facility.

The concept of halo nuclei (see Section 1.2.2) that forms the motivation to study the isotopes in question for Is430 was initially introduced by the Chalmers group through Professor Emeritus Björn Jonson, still active in the group, in 1986 [15, 33].

*Originally *Gesellschaft für Schwerionenforschung*, i.e. “Society for heavy ion research”; now recursively *GSI Helmholtzzentrum für Schwerionenforschung*, i.e. “GSI Helmholtz Centre for Heavy Ion Research”. A research facility primarily concerned with heavy ion research located outside Darmstadt, Germany.

[†]*Facility for Antiproton and Ion Research*: a new international accelerator facility for research with antiprotons and ions, situated adjacent to GSI and using the current GSI facilities as injector stages.

This page intentionally contains only this sentence.

2

Background

This chapter presents some concepts underlying the experiment that is the topic of this thesis. It starts with basic terminology, continues with a quick overview of nuclear reactions and detection mechanisms, a description of the ISOLDE facility and the REX-ISOLDE post-accelerator, before ending with an overview of the detector materials used by the detectors in the experiment.

The terminology and theory mainly coincide with the nomenclature and conventions used in introductory literature by Krane [3], Henley and Garcia [34] and Leo [35].

2.1 Nuclear states

A quantum mechanical treatment of the nucleus renders the concept of discrete *energy levels* in which it can reside. The lowest such energy *state* in a nucleus is known as the *ground state*, and higher levels are known as *excitations*. Excited states tend to reach the ground state via *deexcitation* through different means; commonly by ejecting a photon (a “ γ ” ray) or a particle. The *lifetime* of a state describes a characteristic time duration it “lives” before such a deexcitation occurs. Different processes yield different lifetimes, with the common property that they follow Poisson statistics, i.e. they have “no memory” of how they entered a state or how long they have been in a certain state, which yields an exponential probability distribution for cumulative events.

Of major interest in describing nuclei is their respective compositions of states and their corresponding energy levels. A state is labelled by its angular momentum, which takes a contribution both from the intrinsic *spin* s of the particle (nucleons are spin- $\frac{1}{2}$ particles) and the *orbital angular momentum* l , which sum to the *total angular momentum* j , and sometimes in addition its *parity* π . A notation prototype would be nj_l^π , where n is an ordinal number beginning at 1 which differentiates states that would otherwise have the same notation. In practice the orbital angular momentum is written in spectroscopic notation*, so a sample state could be denoted as $1d_{5/2}^+$ for the first state with $l = 2$, projected

*A historical convention that denotes $l = 0, 1, 2, 3, \dots$ as respectively s, p, d, f and continued alphabetically from there on.

in parallel with the intrinsic spin to yield $j = \frac{5}{2}$ and with positive parity.

One can also assign a spin-parity label to a collective nucleus. The spin in this case refers to its *nuclear spin* I , which in practice is the vector sum of the total angular momentum of its nucleons; the rationale for using the term “spin” is that the nucleus in many ways behaves as if it was a single entity with this corresponding intrinsic spin. Since a single nucleon has half-integer intrinsic spin, which summed with its integral orbital angular momentum yields a half-integral total angular momentum, a nucleus with an even number of nucleons has integral spin and an odd number of nucleons results in half-integral spin.

A nucleus is also given a *nuclear parity* π which is the product of the parities of its individual nucleons. In summary, a nuclear state can thus be collectively described in the form I^π , such as 0^+ for zero total angular momentum and positive parity.

2.1.1 Transitions and selection rules

A key mechanism for a nuclear state to transition from an initial state $I_i^{\pi_i}$ to a final state $I_f^{\pi_f}$ is *photon emission*. This process is governed by several *selection rules* that constrain possible changes in angular momentum and parity. The transitions themselves can be distinguished between *electric* (E) and *magnetic* (M) type transitions in a classical analogue with the fields emanating from electrical and magnetic multipoles, respectively.

The emitted radiation needs to account for the change in angular momentum and parity between the involved states. We index the radiation by its *multipole order* L (the dipole is indexed as $L = 1$), which also corresponds to the carried change in angular momentum by the radiation. Conservation of angular momentum means that the initial, final and carried angular momentum must form a closed vector triangle, which limits the allowed L values. An E transition will be of even parity (which is multiplicatively conserved if “even” is assigned +1 and “odd” -1) if it is of even L and vice versa, and an M transition will be of even parity for odd L and vice versa. Thus, by knowing the nuclear spin and parity of the initial and final state, the possible radiation component types can be deduced.

A special case occurs when $I_i - I_f = 0$: this would, according to the paragraph above, require an $L = 0$ type transition, which would correspond to radiation from a *monopole* field, which does not exist magnetically and cannot occur electrically,* and is thus not allowed. Furthermore, if $I_i = I_f = 0$, we would at the same time *only* be allowed $L = 0$ transitions. This means that e.g. a $0^+ \rightarrow 0^+$ transition is forbidden through electromagnetic radiation.

Apart from electromagnetic transitions, the state can also change via *internal conversion*: a process where an orbital electron is ejected, carrying the difference between the excitation energy and the binding energy of the electron. This creates a natural threshold where the excitation energy must exceed the binding energy of the electron shell in question. If the electron is ejected from an inner shell, higher electrons will rapidly fill its place, which in turn will emit γ rays characteristic for the process.

*The electrical “monopole” is simply a static electric charge which does not radiate.

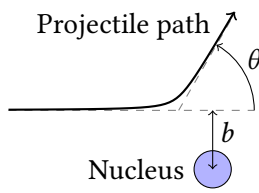


FIGURE 2.1: Illustration of the impact parameter b and the scattering angle θ during a nuclear scattering process. The illustration shows Rutherford scattering in particular, where a positively charged particle is assumed to be deflected solely by the electromagnetic interaction, which yields hyperbolic trajectories due to the inverse square law dependence of the repellant force.

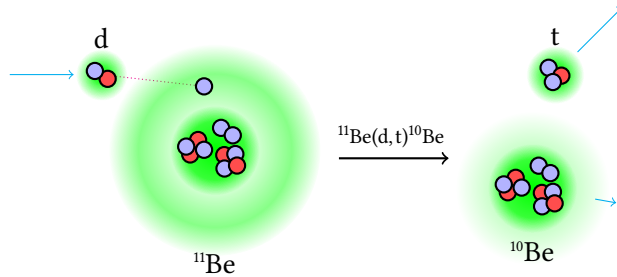


FIGURE 2.2: Illustration of the $^{11}\text{Be}(d,t)^{10}\text{Be}$ transfer reaction in direct kinematics.

2.2 Nomenclature of nuclear reactions

Rutherford's scattering experiment in 1911 mentioned in the introduction is illustrated in Figure 2.1. The process known as elastic *Coulomb scattering* (or indeed *Rutherford scattering*) involves only the electromagnetic interaction, where the positively charged stationary nucleus repels a positively charged projectile. By measuring the distribution of outgoing particles and comparing it with the theoretical models involving the impact parameter, scattering angle and the hyperbolic trajectories for a point-like charged nucleus, Rutherford could by fully classical means deduce the charge distribution of the atom, finding it to contain a small “nucleus” which holds the majority of the atomic mass and all of its positive charge.

The repelling electromagnetic forces stopped Rutherford's projectiles from interacting directly with the nucleus. With the advent of more potent particle accelerators, this boundary could be broken, which yielded events of *nuclear transmutation*, i.e. processes where the isotopes are transformed during the reaction, which enables detailed study of the structure of the particles in themselves. The principle of studying collisions between particles is the foundation for today's field of accelerator based physics, with representatives such as LHC or indeed REX-ISOLDE at CERN.

A reaction involving transmutation can be expressed in the form

$$X(a,b)Y \tag{2.1}$$

where X denotes a target, a a light projectile and b and Y are the reaction products, where b is often a particle ejected from the system and Y a nucleus that remains stationary in the target material. The nomenclature provides a classification of nuclear events, where e.g. a “(d,n)” reaction would describe a reaction where an incoming deuteron (a ${}^2\text{H}$ nucleus) deposits a proton in the reaction and “escapes” as a single neutron. Another possibility is that a is captured in the process and b is a γ ray, denoted as a *radiative capture* event.

2.2.1 Transfer reactions

In a *transfer reaction* in *direct kinematics*, a light *particle* is fired at a heavy *nucleus* (note the contextual usage of the word “particle” for the light bullet, and “nucleus” for the heavy target) where the particle should either deposit a nucleon in a *stripping reaction*, or absorb a nucleon in a *pick-up reaction*. A sample reaction is illustrated in Figure 2.2. By measuring the outgoing angles and energies of the resulting particle(s) and nucleon, information regarding available energy states in the nucleus, particularly the outer orbitals, can be deduced. In fact, capturing only a subset of the resulting entities, combined with energy and momentum conservation, can still yield much information.

If the de Broglie wavelength of the projectile is of the order of the radius of a single nucleon, there is a larger probability for the projectile to interact directly with a nucleon in the outer shells of the nucleus. Such *direct reactions* occur in time frames short enough ($\sim 10^{-22}$ s) that the rest of the nucleus can not notice the reaction immediately, which results in a “clean” interaction with few bodies involved. This simplifies theoretical calculations, which helps when comparing with experimental data to evaluate the success of a certain theoretical model, and can unveil information regarding the overlap between the states of the initial and final nucleus.

When investigating short-lived nuclei, it is often not possible to use a rapidly decaying isotope sample as a stationary target. Instead, the isotope is produced and used as a projectile that impinges on a light target in what is denoted *inverse kinematics*. The physics stays the same by transforming the frame of reference, but the outgoing particles will be differently distributed in the lab system compared to direct kinematics.

2.2.2 Compound reactions

When a nucleus is approached by a projectile with a small impact parameter (compared to the nuclear radius — see Figure 2.1) and a de Broglie wavelength at the size of the nucleus rather than a single nucleon, the projectile is more likely to interact with the nucleus as a whole in a *compound reaction* instead of just a single nucleon in an outer shell, with possibly additional immediate collisions between the constituents of the system. In such a process (lasting about 10^{-18} s to 10^{-16} s), the system enters a definite intermediate state consisting of an excited *compound nucleus* which in turn can decay in any energetically

available channel allowed by conservation laws. Even though the average increase in nucleon energy in such a state might not be sufficient to overcome the nucleon escape energy from the nucleus, the statistical energy distribution from internal collisions may result in a nucleon momentarily obtaining enough energy to “evaporate” away from the nucleus. With increasing compound excitation energy, even multi-particle ejections become possible.

In this excited state, the nucleus no longer has any “memory” of the process that produced the state and will, for a relatively light incident particle, characteristically not show any angular preference for possible outgoing products in the centre-of-momentum frame. This lack of memory destroys any reaction information not pertaining pure conservation laws.

2.3 Nuclear reaction kinematics

Conservation of energy before and after a basic nuclear transfer reaction as in Section 2.2.1 (currently neglecting excited states) produces the relation

$$m_X + T_X + m_a + T_a = m_Y + T_Y + m_b + T_b \quad (2.2)$$

where m denotes rest mass, T kinetic energy and the indices are as defined in Equation (2.1).

The Q value for the reaction is defined as the mass difference between the initial and the final products, which via Equation (2.2) is seen to exactly balance the difference in kinetic energy between the final and the initial state:

$$Q = m_{\text{initial}} - m_{\text{final}} = T_{\text{final}} - T_{\text{initial}}. \quad (2.3)$$

The Q value thus denotes the amount of energy released by the reaction. Borrowing nomenclature from thermodynamics, a reaction is called *exothermic* if $Q > 0$, and *endothermic* if $Q < 0$.*

*In this case the reaction rather absorbs than releases energy.

At the same time, a general expression of conservation of linear momentum gives

$$\vec{p}_X + \vec{p}_a = \vec{p}_b + \vec{p}_Y \quad (2.4)$$

which in this general form is valid in any frame of reference.

Looking specifically at the frame where X is at rest, which corresponds to the laboratory frame in our transfer reaction, and decomposing the vector equation into two planes: one containing the incident beam and the resulting particles (symmetry in the final linear momentum distribution ensures that the respective trajectories of Y and b will describe

the same plane) and a perpendicular complement, yields the relations

$$p_a = p_b \cos \theta_b + p_Y \cos \theta_Y \quad (2.5)$$

$$0 = p_b \sin \theta_b - p_Y \sin \theta_Y \quad (2.6)$$

where θ_b and θ_Y denote the angles between the beam direction and the b and Y entities respectively.

By assuming knowledge of the beam energy, this leaves five unknowns – angles and energies of b and Y and the reaction Q value – related by Equations (2.2), (2.5) and (2.6). Since the heavy resulting product Y in a regular transfer reaction experiment will typically remain trapped in the target (or be sent to a beam dump in reverse kinematics) and thus not be detected, a reasonable first step is to eliminate T_Y and θ_Y . Using the low-energy non-relativistic approximation $T = mv^2/2$, the remaining relation can be expressed in the kinetic energy of the resulting particle b as [3, Equation (11.5)]

$$\sqrt{T_b(Q, \theta_b)} = \frac{\sqrt{m_a m_b T_a} \cos \theta_b \pm \sqrt{m_a m_b T_a \cos^2 \theta_b + (m_Y + m_b)(m_Y Q + (m_Y - m_a)T_a)}}{m_Y + m_b} \quad (2.7)$$

which can be used to compare energy/angle relations in an experiment with known Q values to identify reaction channels. Conversely, if we instead measure T_b and solve the equation for Q , the relation can be used to find the Q value which via Equation (2.3) can determine e.g. a previously unknown mass component.

If the reaction products reach excited states of energy E_{ex} , the Q value in Equation (2.7) should be replaced by a modified value Q_{ex} defined as

$$Q_{\text{ex}} = Q - E_{\text{ex}} \quad (2.8)$$

where Q is seen to correspond to the correct value when only the ground state is reached.

A final note is that since the equation in itself does not label which of the resulting constituents is light or heavy, switching all indices from b to Y and vice versa in Equation (2.7) produces an identically valid formula for the heavy fragment, which can be of use in inverse kinematics if the heavy fragment can be detected.

2.4 Detection principles

Electronic detection of nuclear radiation (particles or γ events) relies on the radiation interacting with the detector material, losing energy in the process while releasing electrons that are collected and turned into an analysable pulse. Requirements in the form of differing particle types to detect, energy ranges, intensities, granularity in time, energy and space, etc., demand different detector materials and geometries, not least governed by eco-

nostic factors. A short write-up on the principles behind the detectors in the performed experiment follows.

2.4.1 Charged particles

When an electromagnetically charged particle travels through a material, it will to a predominant degree collide with electrons rather than nuclei, due to the general atomic composition of a small heavy nucleus surrounded by an electron cloud with a volume about 15 orders of magnitude larger [3]. The energy loss mechanisms differ to some degree depending on the relative mass between the incoming particle and the colliding electron.

If the incoming particle itself is an electron, i.e. of the same mass as the colliding bodies, it can be heavily deflected from its path during such a collision. Furthermore, interesting electrons, from e.g. β^- decay, will often travel at relativistic speeds, which in combination with the large velocities involved can make *bremstrahlung** significant.

In contrast, the inertia of a relatively heavy charged particle (e.g. a proton which is almost 2000 times heavier than an electron) ensures that it will follow a rather straight line in the detector while undergoing a large number of electron interactions picking away the kinetic energy. The lack of large accelerations compared to the detection of an electron mentioned above makes radiative losses negligible, and the statistics behind the large amount of collision events ensures that the particle will have a characteristic *range* in a medium, dependent on the incoming energy and particle type.

For heavy charged particles which are the focus of this experiment, an expression for the energy loss per unit length was found by Bethe in the expression [3, Equation (7.3)]

$$\frac{dE}{dx} = \left(\frac{e^2}{4\pi\epsilon_0} \right) \frac{4\pi z^2 N_A Z \rho}{m_e c^2 \beta^2 A} \left[\ln \left(\frac{2m_e c^2 \beta^2}{I} \right) - \ln(1 - \beta^2) - \beta^2 \right] \quad (2.9)$$

where

- c , e , N_A and ϵ_0 are the speed of light in vacuum, elementary charge, Avogadro constant and vacuum permittivity
- βc and ze are the velocity and electric charge of the particle
- Z , A and ρ are the atomic number, atomic weight and density of the detector material
- m_e is the electron mass
- I is the mean excitation energy of the atomic electrons, which in theory could be calculated, but in practice is tabulated for different materials with a typical value of about $10Z$ expressed in electron volts.

*Radiative losses inevitably experienced by accelerated charged particles.

The finite energy loss per unit length $\Delta E/\Delta x$ can be measured by letting a charged particle hit an energy detector thin enough to let the particle punch through. By combining this with a thicker subsequent energy detector that registers the remaining kinetic energy, both the energy loss per unit length and total energy can be measured for a single event.

The main result of Equation (2.9) in this context is the $\propto z^2/\beta^2$ dependence for non-relativistic energies ($\beta \ll 1$), where the expression in the ending brackets will stay close to constant with changing particle velocity. Using the approximate $E = mv^2/2$ relation for the kinetic energy of non-relativistic particles, the energy loss proportionality relation can also be expressed as

$$\Delta E = C \frac{z^2 m}{E} \quad (2.10)$$

where m is the mass of the incident particle and C is a constant for the ΔE detector in question.

By Equation (2.10), a plot of ΔE against E for an event should place it on a hyperbola scaled as $z^2 m$, thus allowing particle identification with a known particle reference, or by inferring particle types from the experimental conditions.

2.4.2 γ rays

Detection of the mass- and chargeless photon happens through essentially different processes compared to the charged particles in Section 2.4.1. The interaction is split into primarily three distinct processes that each dominate a certain region defined by photon energy and proton number Z of the absorbing material (see Figures 2.3 and 2.4).

In the low-energy, high- Z region, the reaction is dominated by the *photoelectric effect*, which involves absorption of a photon by an atom which in turn ejects one of its previously bound electrons with an energy corresponding to the difference between the incoming photon energy and the binding energy of the electron in question (see Figure 2.4a). This absorption process cannot occur with a free electron while conserving both energy E and momentum p : in a frame where the free electron would initially be at rest before absorbing the momentum of the incoming photon, relativistic energy conservation would together with the photon relation $p_\gamma = E_\gamma/c$ yield

$$E_\gamma + m_e c^2 = \sqrt{E_\gamma^2 + (m_e c^2)^2} \quad (2.11)$$

which is not valid for non-zero photon energy. If the electron were bound in an atom, however, the nucleus could absorb part of the momentum to allow the process.

As incoming energy increases and/or Z decreases, *Compton scattering* takes more precedence, where the incoming photon scatters inelastically against a loosely bound atomic electron (see Figure 2.4b). This results in a lower-frequency photon with the electron car-

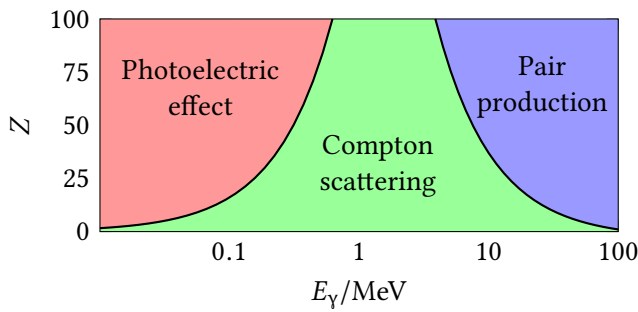


FIGURE 2.3: Qualitative scheme over the dominant regions for the different matter interaction processes for photons depending on photon energy E_γ and proton number Z of the detector material.

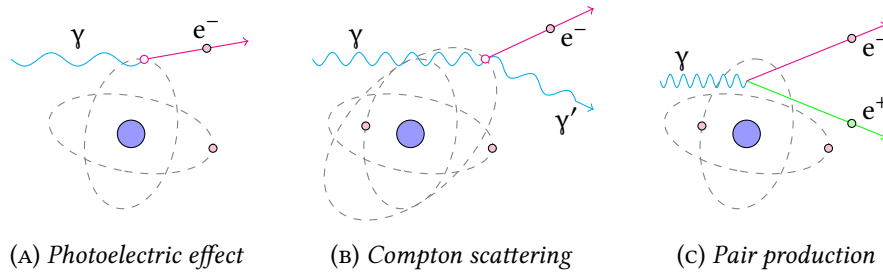


FIGURE 2.4: Illustrations of matter interaction processes for photons.

rying the difference in energy.

For a photon with energy larger than $2m_e$, where $m_e = 511$ keV is the electron rest mass, there is a possibility of *pair production* — a process where the photon transforms into an electron–positron pair (see Figure 2.4c). Analogously with previous cases, this demands a nearby nucleus to absorb momentum in order for the conservation laws to hold.

2.4.3 Neutrons

Due to their lack of net electromagnetic charge, neutrons do not produce any directly ionising events that can be collected and measured. In practice detection is performed by looking at secondary effects of letting a neutron hit a nucleus, with results such as:

- *elastic scattering* against charged particles in the detector material, whose recoil will in turn create ionising events
- *absorption* of the neutron by a nucleus that subsequently produces energetic charged particles that ionise the material
- *activation*, where the neutrons are captured by a nucleus, leaving it in an unstable configuration that decays through a channel to produce detectable events.

Which method is employed in a certain experiment depends to a large part on the expected neutron energy range.

The most favourable elastic scattering event in terms of maximum energy loss occurs for head-on collisions with a charged particle with similar mass, for which a proton is the perfect prototype. This would in theory enable full energy transfer to the proton, which in turn ionises the material. The distribution of impact parameters for different incoming trajectories will in practice generate a distribution of energy transfer coefficients for the collisions. For a proton collision, the neutron will transfer on average half of its energy, with this fraction going down for heavier nuclei. A 1 MeV neutron will require on average 26 collisions to become a *thermal neutron** in collisions with ^1H nuclei, but e.g. over 2000 in collisions with ^{238}U [36]. Detection via elastic collisions is thus best achieved with a hydrated target.

*A neutron in thermal equilibrium with “room temperature” at 17°C will most likely have the energy 0.025 eV, and is then denoted a “thermal neutron”.

The absorption cross sections for thermal neutrons are very large for several commonly used detector materials, with the cross section typically following a $1/v$ dependence at higher neutron velocities v without much deviation up to about 100 keV. At even higher energies, different reaction *resonances* – specific energies which manifest a sudden and dramatic increase in the cross section – become relevant, producing a more complex pattern. These resonances can be used to counter the general inverse dependence on neutron energy for the cross section, enabling capture of useful statistics at least at certain well specified energies. By comparing the actual absorbed amount of neutrons with known cross sections, information on the distribution can then be obtained.

Germanium interaction

The germanium isotope ^{72}Ge , constituting 28 % of naturally occurring germanium, has the uncommon property that its ground state and first excited state are both 0^+ [2]. Selection rules for state transitions therefore disallow radiative deexcitation from the first excited state and leaves the process exclusively up to internal conversion (see Section 2.1.1 for a quick review of the selection rules). The electron will receive a characteristic energy of 690 keV and be ejected after a mean lifetime of $\tau = 444.2(8)$ ns [2, 37], which is several orders of magnitude larger than a typical γ deexcitation in the order of picoseconds. The low-lying energy levels of ^{72}Ge are illustrated in Figure 2.5.

A neutron with an energy above the excitation energy of the first excited state in ^{72}Ge can thus be indirectly detected by looking at the characteristic 690 keV signal that follows the inelastic scattering of such a neutron, especially by loosening the coincidence timing criteria to include the mean lifetime of the state. If there are multiple processes capable of exciting this state, the neutron variety could be distinguished further by pulse shape analysis, selecting events that follow a signal from a recoiling ^{72}Ge nucleus.

It is of note that neutron interaction is generally seen as a nuisance in germanium detectors where it can degrade the detector response for interesting events (most commonly γ rays) [2]. Using this unavoidable reaction channel to actually detect the neutron could

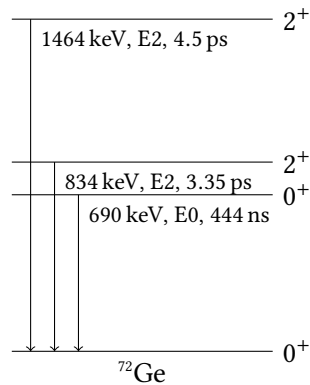


FIGURE 2.5: Scheme of the low-lying energy levels of ^{72}Ge .

have applications in monitoring the rate of these events during an experiment to avoid degradation of the detectors in question.

2.5 Beryllium

With its low atomic number of 4, beryllium was early thought of as a natural and crucial waypoint in *stellar nucleosynthesis*: the process in which lighter elements are fused into heavier elements by being subjected to the conditions within stars. Going from protons to the abundant ^{12}C nucleus could in theory pass through a combination of α nuclei such as $2\alpha \rightarrow {}^8\text{Be}$ and ${}^8\text{Be} + \alpha \rightarrow {}^{12}\text{C}$. However, ${}^8\text{Be}$ is unstable with a lifetime in the order of 100 attoseconds and astronomer Fred Hoyle realised in the early 1950s that a process via that isotope would not by itself be sufficient to produce the amount of ^{12}C present in the universe. The “rescue” lay in the postulation and later finding of a certain resonance in ^{12}C which makes the combining of three α nuclei into carbon in the *triple- α process* significantly more likely than it initially might look.

Being part of basic nucleosynthesis has spawned general examinations of the element, but they are in part hindered of beryllium being *monoisotopic*, i.e. there is only a single stable isotope, which in this case is ${}^9\text{Be}$. Half-lives of different isotopes of beryllium are listed in Table 2.1. The short half-lives of the non-stable isotopes (with the notable exception of ${}^{10}\text{Be}$) put special conditions on possible experiment methods to use.

As noted in Section 1.2.2 and Figure 1.2, ${}^{11}\text{Be}$ is a one-neutron halo nucleus. In that vein, it can further be noted that also ${}^{14}\text{Be}$ is a halo nucleus, commonly denoted as a two-neutron halo nucleus with the structure of ${}^{12}\text{Be} + 2n$, though a four-neutron halo structure has not been ruled out [38].

TABLE 2.1: Halflives of beryllium isotopes ordered by number of neutrons N [3, 10].

N	$t_{1/2}$
7	53.3 d
8	70 as
9	<i>Stable</i>
10	1.39 My
11	13.8 s
12	21.5 ms
13	2.7 zs
14	4.35 ms
15	< 200 ns
16	< 200 ns

2.6 Beam delivery

The creation of the exotic beam at ISOLDE starts with bombardment of a production target with accelerated protons, which on impact create a variety of isotopes that in turn are extracted and accelerated. A short run-down of the process follows. The information in this section is in general based on overview articles by Lindroos [39], Kugler [40] and Habs et al. [41].

2.6.1 Proton acceleration

To obtain protons, hydrogen atoms from a bottle of hydrogen gas are ionised and handled by the initial linear accelerator Linac 2. As the charged particles travel, they are subjected to alternating electric fields, tuned to vary between pushing and pulling the protons at a frequency that result in an accelerated current. At the end of Linac 2, the protons have obtained a kinetic energy of 50 MeV.

The protons are delivered to the PS Booster (“Proton Synchrotron Booster”) which increases the proton energy further by applying tuned electric and magnetic fields in a circular accelerator. By its nature, a synchrotron collects the particles in “bunches”, which are delivered at a final energy of 1.4 GeV to further acceleration facilities at CERN for use in high-energy experiments, or to the initial section of the ISOLDE experiment hall.

The bunches from PS Booster generally come at a repetition time of 1.2 s, which is a first constituent of the general time structure for ISOLDE experiments.

2.6.2 The ISOLDE facility

The accelerated proton beam is directed to a thick production target made of heavy isotopes, where a spectrum of new isotopes is created. By hitting the heavy targets, they can eject nuclear constituents either in a direct spallation process or by reaching excited states resulting in fission to lighter elements. These products diffuse out of the heated target where they can be subjected to the “Resonance Ionization Laser Ion Source”, *RILIS*, which ionises the isotopes with a high elemental selectivity before they are lifted and accelerated by an applied electric field.

By subjecting the products to a bending magnetic field, a selection can be made depending on the charge-to-mass ratio of the isotope. ISOLDE has two such facilities: the “General Purpose Separator” (GPS) and the “High Resolution Separator” (HRS). The smaller GPS uses a single bending and focusing magnet and can simultaneously deliver three different isotopes to different experiments. The HRS uses two bending magnets with additional magneto- and electrostatic elements for higher order corrections to achieve a mass resolving power of up to 15 000, compared with 2400 for the GPS.

At the end of this process, the selected isotopes are delivered in a bunched structure at about 60 keV. To perform nuclear experiments of the type described in this thesis, they need to be further accelerated to obtain an energy in the MeV range, which is the task of the REX-ISOLDE setup.

2.6.3 REX-ISOLDE

Since 2002, the “post-accelerator for Radioactive beam EXperiments at ISOLDE”, *REX-ISOLDE* for short, has performed the task of further accelerating the isotopes produced at the separators and creating a useful beam structure for use in different nuclear experiments. This process consists of several steps, briefly described below. A more detailed view of the process is given by Habs et al. [41], of which this section is a partial summary. Frequent references can be made to Figure 2.6.

REXTRAP

As a first step in the acceleration process, the isotopes are actually decelerated from the delivered 60 keV to just a few eV by encountering an electric potential barrier at *REXTRAP*— a Penning trap with the purpose of accumulating, cooling and purifying the beam before further delivery.

After the initial deceleration, the beam enters the Penning trap where it is subjected to a strong magnetic field at 3 T and subjected to further frictional energy losses in collisions with a *buffer gas* within the trap.

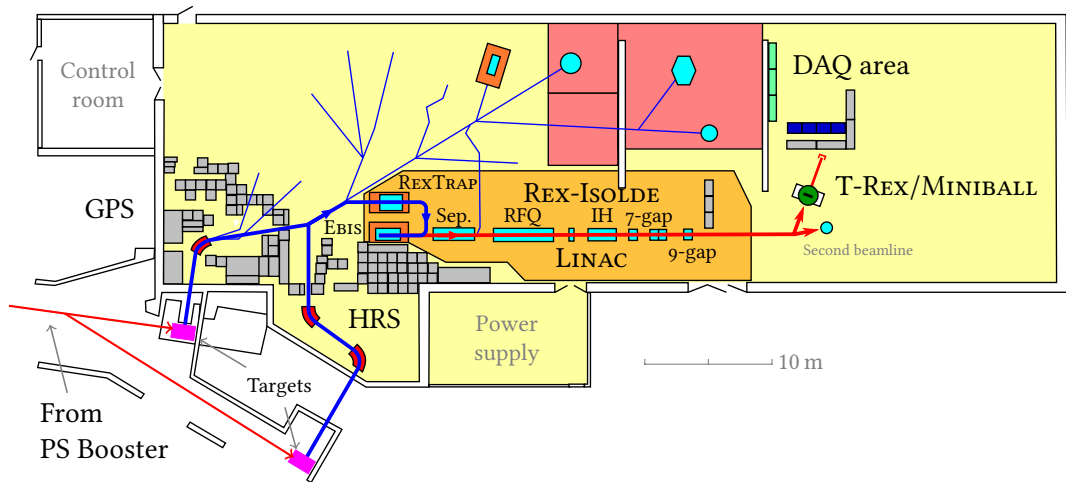


FIGURE 2.6: Schematic of the ISOLDE hall in general and REX-ISOLDE in particular.

The Penning trap design allows for another isotope selection process, where contaminants from the separator stage can be further reduced, and the cooling enhances the beam characteristics for experimental use before it is delivered to the next part of the REX-ISOLDE chain.

REXEBS

Since the performance of electric acceleration of charged isotopes is directly proportional to the charge, it is favourable to ionise as far as possible before the acceleration stage. In this next stage, the beam is trapped radially in a potential well by encountering a focused electron beam in the “REX Electron Beam Ion Source”, *REXEBS*. This electron beam at 0.5 A strips electrons from the ion beam by collisions while the beam simultaneously is confined longitudinally by an electric field. To extract the beam, the electric field is reversed in short pulses at the *EBIS pulse frequency*, which is typically set to 49 Hz, delivering bunch lengths of $< 100 \mu\text{s}$ at intervals of about 20 ms.

Further mass separation

The buffer gas from REXTRAP will travel along the beam as a contaminant, overwhelming certain interesting beam isotopes to several orders of magnitude at this stage. Further mass separation is needed to keep the beam clean before the experiment chamber.

For this reason, REXEBS is followed by a mass separator, where care needs to be taken to not destroy the useful beam characteristics that the earlier steps have generated. This is accomplished by a combination of magnetic and electrostatic bending portions in a double-

focusing mass spectrometer, where the dispersive effects of both fields are designed to cancel, keeping the beam in relative focus [42]. The construction reaches a mass selection factor $\Delta m/m$ of 1/150, which is deemed to be necessary to create beams sufficiently pure for experimental purposes.

Acceleration

A final linear accelerator consisting of several stages takes the beam to the energies needed for the experiment in question. This produces yet another time structure for the beam on the order of nanoseconds (the exact frequency depends on the final energy) and yields a final beam energy of up to 3 MeV/u, delivered into the experiment chamber.

Upgrades

As of writing, an upgrade called *HIE-ISOLDE* is under way, which will raise the maximum deliverable energy to initially 5.5 MeV/u in Q2 2015, continuing to 10 MeV/u in 2016–2017, increase beam quality and make a larger range of isotopes available [43, 44].*

*Approximate time frames updated as of printing this thesis through personal communication with Professor Thomas Nilsson

2.7 Semiconductor detectors

The information in this section mainly comes from introductory literature by Krane [3] and Leo [35].

An early detection technology for nuclear radiation consisted of *gas-filled counters*, which operated on the principle that radiation would enter an *ionisation chamber* and ionise the gas molecules therein. An applied voltage would accelerate the ions towards one of the electrodes, on their way starting an *avalanche* of *secondary ionisations* that could be collected. The amount of detected ionisation events could then within a certain range be proportional to the incoming energy of the radiation. Disadvantages include the possibility of *secondary avalanches*, where photons produced by the secondary ionisations would in turn be picked up as radiation events in other parts of the detector and in practice trigger ionisation of the entire chamber. It would then no longer be possible to deduce the incoming radiation energy, only leaving information on the existence of an event.†

†This process is in itself used in Geiger counters, with advantages in simplicity and portability.

Apart from the limited useful energy ranges for gas-filled proportional counters, they also suffer the drawback of being impractical for detecting a large spectrum of interesting events due to low efficiency for e.g. high-energy γ rays — as a comparison, a 1 MeV photon has a range of about 100 m in air. To counter this, solid detector bodies would be useful to provide dense bulk material for reactions. Wanted properties would be high electron mobility to achieve good energy resolution, but at the same time limited conductivity to form well-defined pulses and minimise background noise. This means that the material

should behave both as a conductor and an isolator, which might seem like a paradox, but technological advancements in the late 1960s enabled such properties to be combined in a specific way with the advent of semiconductors.

The advantages of semiconducting detectors were quickly realised, but their relatively high cost hindered adaptation. With time, however, the broad field of application for semiconductors triggered research and lowered prices, and they are today widely used in nuclear and high energy physics.

The high material density compared to gas-filled detectors enables a semiconductor detector to be more compact and still pick up penetrating radiation. They also provide substantially improved energy resolution, working ranges and response times. Disadvantages include a higher cost, degradation from radiation damage to the crystalline structure and in certain cases the necessity of complex cooling to avoid thermal disturbances crossing the band gap.

2.7.1 Materials used

Semiconducting properties are found in many pure elements and compounds, but in practice mainly two varieties – silicon and germanium – are used for detectors, with respective working domains.

Silicon

The properties that make silicon widely used in consumer-grade electronics also make it the most commonly used semiconducting material for charged particle detection. Production processes are mature, availability is high and in contrast to several other semiconducting materials, silicon fares well in room temperature conditions.

Drawbacks for detector purposes include difficulties to produce large functioning areas of pure silicon, which limit single devices to detection areas of order 10 cm^2 . This also impacts the thickness of the workable depletion zone, which directly limits the stopping power and thus which event types that can be fully captured and measured.

Germanium

The band gap in a germanium based semiconductor is much narrower than in silicon, to the point that thermal excitations at room temperature exceeds it. For noise-free and usable operation, germanium detectors are thus in practice cooled to liquid nitrogen temperatures ($-196\text{ }^\circ\text{C}$). To obtain larger crystals it used to be common to use lithium-drifted germanium, known as Ge(Li) detectors, which needed to be kept cool not only during operation, but at *all* times to avoid the high mobility of the lithium ions from permanently degrading the crystals. Today there are improved methods to create larger pure germanium crystals, also

known as *intrinsic germanium* or *high purity germanium* (HPGe), that do not necessarily need this constant cooling outside of operation time, but they still require more intricate handling than silicon detectors.

Despite these inconveniences, germanium detectors are widely used for γ spectroscopy. Both the ability to create larger effective detector volumes and the higher proton density of germanium compared with that of silicon make photoelectric interaction much more likely at similar energies (see Figure 2.3), which allows efficient detection over a larger energy range and with improved resolution.

2.7.2 Position detection for charged particles with DSSSDs

A technique for determining the position in space for an incoming charged particle is to create a *pixel grid* by covering one side with electrode *strips* in a certain configuration, and the other with similar strips in non-parallel directions with the first. If the incoming charged particle penetrates the front strip detectors to also be detected in the back, it is then possible to determine the 2D pixel where it hit.

One such construct using semiconducting silicon strips is known as a *double-sided silicon strip detector* (DSSSD) [45]. If it can be deduced that the particle fully penetrated the DSSSD, known as a *punch-through event*, the combined energy signals describe the fractional energy loss ΔE over the detector.

2.7.3 Particle identification

The ΔE detection mechanism noted above is one part of the particle identification scheme mentioned in Section 2.4.1. The other is finding the total energy, which can be achieved by placing a thicker silicon *pad detector* behind the DSSSD grid detector. If the particle can be fully stopped in the pad detector, its total remaining energy can be measured. Summed with the energy lost in the DSSSD, this yields the total energy E , which should place the event on the mentioned hyperbolas in a ΔE against E plot depending on particle type and DSSSD characteristics.

Material variables such as detector thickness, and electronic variables such as signal amplification, need to be tuned for the expected relevant particles wanted for study to achieve a clear separation of ΔE values and a high probability of punch-through events.

This page intentionally contains only this sentence.

3

Experiment

Since the halo neutron in ^{11}Be described in Section 1.2.2 is weakly bound and thus likely to cleanly interact in a collision, transfer reactions as described in Section 2.2.1 is a favourable method for study of this isotope. The short half-life of ^{11}Be demands using this exotic isotope as the beam in an inverse kinematics configuration, which provides a rationale for the choice of this method in Is430

This chapter will present the experimental conditions and processes that produced the experimental results. The information reference is to a large part the thesis by Johansen [46], but also the actual measurement data used to produce this thesis and personal notes from the experiment itself.

3.1 Run configuration

3.1.1 Beam

The beam isotope used was ^{11}Be , which is characterised as a one-neutron halo nucleus [16]. It was produced in the ISOLDE facility, using the GPS (see Section 1.3.1) and a Ta target, and post-accelerated by REX-ISOLDE (see Section 2.6.3). The ^{11}Be half-life of 13.4 s as noted in Table 2.1 is an order of magnitude longer than the timescale between beam production, extraction and impact described in Section 2.6, and should not be an influential factor in the analysis (this assumption is affirmed in Section 4.1.2). The isotope is created in the beam production target on proton beam impact, which occurs on the order of every second. The beam is delivered from the EBIS into the target chamber at 49 Hz, i.e. about every 20 ms, as noted in Section 2.6.3.

The timing characteristics of several processes during the beam production combine to produce a “pseudo-constant” beam, whose intensity will vary in time in non-trivial ways [47]. This will need to be taken into account wherever found relevant.

The beam energy is given by the REX-ISOLDE accelerator at 2.85 MeV/u, which amounts

to approximately 31.35 MeV for ^{11}Be . Verification attempts through energy and momentum conservation of kinematically determined events in the experimental data indicate this figure to be consistent within experimental errors [46, Section 6.3].

By inserting dedicated intensity measurement runs in between the main experiment runs (see Section 3.1.2), the beam intensity averaged over a typical run time was seen to fluctuate noticeably during the experiment. The intensity between the dedicated intensity measurement runs was deduced by constructing the ratio between the measured incoming beam intensity and the intensity of detected deuterons in the experimental run adjacent to the dedicated measurement run. With the assumption that the beam intensity would stay close to constant between these adjacent runs, the deuteron intensity and the calculated ratio could then be used to recover the beam intensity during the runs between direct intensity measurements. The intensity was found to vary between $6.12 \cdot 10^6/\text{s}$ to $4.46 \cdot 10^6/\text{s}$, slowly dropping during the experiment.

3.1.2 Targets and sources

The target the ^{11}Be impinged on consisted of deuterated polyethylene (CD_2) with the intent of studying reactions between the beam and the deuterons. In addition, a regular polyethylene (CH_2) and a pure carbon target were used to gain information on events hitting either carbon nuclei or some of the present hydrogen impurities in the CD_2 .

A silver target was used to measure the beam intensity in the reaction chamber. The given beam energy and charge impinging on silver – in contrast with the other targets used – should never break the Coulomb barrier and thus the detected event distribution should directly correspond to the known Rutherford scattering process, yielding the absolute intensity. To account for fluctuating beam intensities during the run, silver runs were inserted at regular intervals in the experiment set.

Consumer-grade aluminium foil was used as another chamber target. The thickness was approximated to be $200\ \mu\text{m}$ by wrinkling a foil sheet of known area into a ball and weighing it – a more precise figure was not important for its purpose. The ^{11}Be isotopes from the beam were stopped in the foil to subsequently β^- -decay to excited states in ^{11}B , that in turn quickly γ -decay with known energies. This in practice becomes a stationary ^{11}Be source and was used to calibrate energy and efficiency of MINIBALL: the germanium detector in the experiment (see Section 3.2.1). For the same purpose, there were additional runs with stationary samples of the radioactive isotopes ^{60}Co , ^{152}Eu and ^{207}Bi to generate denser calibration points over a larger energy interval.

The used chamber targets are listed in Table 3.1.

TABLE 3.1: Targets used in the experiment. Thickness data from Johansen [46, Table 4.1].

Target	Thickness /mg cm ⁻²	Primary purpose
CD ₂	1.00(5)	Primary target for beam+deuteron reactions.
CH ₂	1.1(1)	Background measurements from beam+proton reactions.
C	1.50(5)	Background measurements from beam+carbon reactions.
¹⁰⁷ Ag	1.9(1)	Beam intensity measurements via Rutherford scattering.
Al	54	Energy and efficiency calibration of MINIBALL.

3.1.3 Runs

A single run lasted until 2 GiB of detector data had been collected, which generally corresponded to 50 min for an uninterrupted primary run, up to 2 h 30 min for a lower count run. Each run was given an incremented identification number which was recorded together with information such as chamber target used, run length and other run parameters for use in the subsequent analysis.

The experiment gathered in total about 300 GiB of experiment data over a period of five days.

3.2 Detectors

The detector setup is a combination of MINIBALL and T-REX, described in this section. Refer to Figure 3.1 for a visual representation of their configuration.

3.2.1 MINIBALL

The γ detector in experiment Is430 is the highly segmented germanium detector MINIBALL (see Figure 3.1). It consists of 8 detector clusters, positioned like the corners of a six-sided dice facing its centre, each with 3 respective germanium crystals electronically segmented in 6 sections, for a total of 144 individual recording segments [53].

The energy resolution of MINIBALL for γ rays at 1 MeV is on average below 3 keV [54], with a detection efficiency in the T-REX configuration of 5.0(3) % at 1332 keV [48].

3.2.2 T-REX

The target chamber is surrounded by the T-REX (“Transfer at REX”) silicon detector [48] which effectively shields MINIBALL from charged particles resulting from the chamber reaction (see Figure 3.1). T-REX consists of a structure radially surrounding the beam, split into the *forward barrel* and *backward barrel* with direction reference to the target spot and

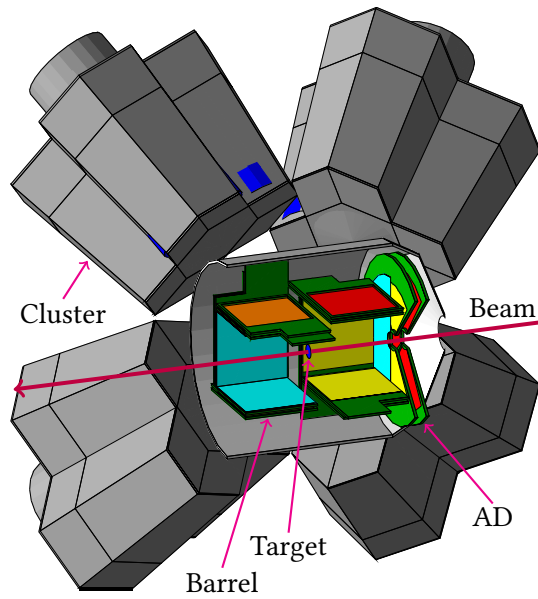


FIGURE 3.1: Cutaway rendering of the T-REX and MINIBALL configuration. Refer to the text for information concerning the parts. The front AD and the left sides of the T-REX barrel, the MINIBALL array and the vacuum chamber have been cut away for clarity. The image includes the back AD, which was not present in *Is430*. The target is mounted on a “ladder” which is inserted into the chamber. The rendering is exported from the simulation model of the T-REX setup [48] which extends the *g4miniball* package [49] created for use with the *Geant4* simulation software [50, 51]. The export is used with the permission of Wimmer [52].

beam direction, capped off with annular detectors denoted the *front AD* and *back AD* which are hollow at the origin to let the beam through. In Is430, the back AD was not present due to theoretical considerations rendering it unnecessary since no events of interest would occur in its angular coverage. The T-REX configuration used covers θ -angles from 8° to 152° as measured from the target with reference to the beam direction.

Each segment of T-REX consists of a DSSSD acting as a ΔE and position-sensitive detector that sits in front of a pad detector for registering the full event energy to enable particle identification (see Sections 2.7.2 and 2.7.3).

The particles of interest for the T-REX setup in this experiment are mainly light charged particles such as protons, deuterons and tritons. However, there is also generally a possibility for energetic heavy fragments from the beam to be deflected far enough to hit the front AD, which is constructed to withstand such events, and in this experiment also the forward barrel. To protect the semiconducting characteristics from these heavy fragments, the forward barrel was shielded with a $11.57\ \mu\text{m}$ thick BOPET foil,* which should fully stop heavy fragments in an application of the Bethe equation (see Section 2.4.1). A negative side-effect of this approach is that the lighter particles that are meant to pass through still struggle to some extent in the foil, losing energy approximately proportional to the effective distance they travel through the foil depending on incident angle. This needs to be compensated for to be able to clearly distinguish between particle types in the $\Delta E-E$ analysis, as done by Johansen [46]. Another effect is that it increases the low-energy limit for particles being able to traverse the ΔE detector to produce a fully analysable event. Neutrons and γ rays, however, are not disturbed to any relevant extent by the foil.

* *Biaxially-oriented polyethylene terephthalate*: a polyester film commonly sold under brand names such as “Mylar”.

3.3 Detector calibration

3.3.1 MINIBALL

Energy calibration of MINIBALL utilised known decay mechanisms of a stationary ^{152}Eu source and the experiment beam hitting a stopper foil target for subsequent deexcitations within the chamber. This calibration was performed by Johansen [46, Section 5.6.1].

Positional calibration for the individual segments of MINIBALL was done by utilising a $d(^{22}\text{Ne}, p)^{23}\text{Ne}$ reaction. By gating on proton detection in T-REX and looking at γ detection from the $\frac{1}{2}^+ \rightarrow \frac{5}{2}^+$ transition in ^{23}Ne with known energy, the angle of the segments could be deduced through analysing the observed Doppler shift. This calibration was performed by Johansen [46, Section 5.6.2].

Detection efficiency was determined through radioactive ^{152}Eu and ^{60}Co sources using known γ energies within 100 keV to 1400 keV. This was performed by Wimmer [52, Section 4.1.1].

The polar angle distribution of the 144 recording segments in MINIBALL is not even (see

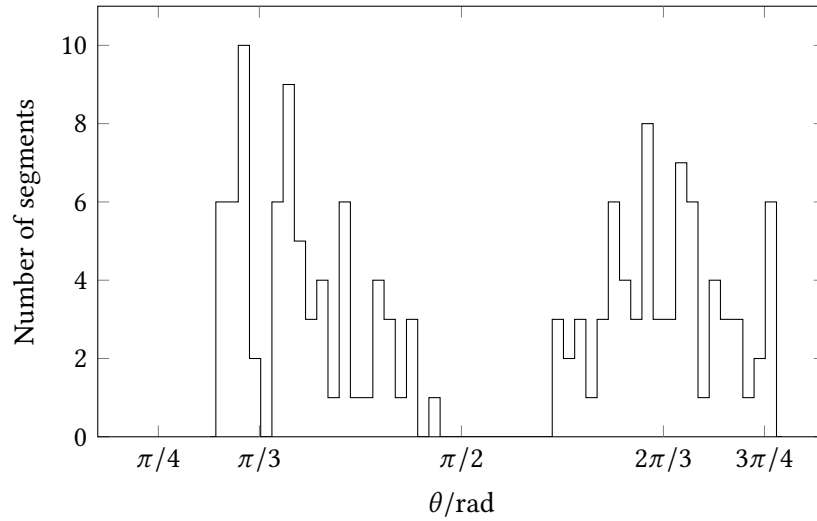


FIGURE 3.2: Polar angle θ distribution of the segments in MINIBALL. The angle is defined with respect to an origin in the chamber target spot, measured from the axis defined by the positive beam direction (i.e., $\theta = 0$ coincides with the beam dump).

Figure 3.2). The lack of symmetry will reflect in recorded count rates, and angular distributions from signals recorded in MINIBALL needs to be viewed in light of this geometry.

3.3.2 T-REX

The energy calibration of the T-REX constituents was performed by inserting radioactive α -sources (^{148}Gd , ^{239}Pu , ^{241}Am and ^{244}Cm) in the target position and comparing the raw recorded energy spectrum with known decay energies. This was performed by Johansen [46, Section 5.3–5].

The positions of the individual strips and rings of the AD and the barrel in relation to the laboratory frame were determined from known construction parameters of T-REX [46, Section 5.2].

3.4 Data capture and processing

**“MBS and ROOT Based Online/Offline Utility”.

The data acquisition setup at REX-ISOLDE uses the MAR_qB_QU* system [55], which in turn uses the “Multi Branch System” (MBS) [56] for data readout, event building and data transport, and the ROOT framework [57] for the graphical user interface and data storage.

The experiment data is initially recorded in an “MBS Event Data” (MED) structure [58] on disk. This file is later unpacked into separate native ROOT trees, corresponding to the different phases of the experiment (e.g. when the beam is deemed to be hitting the target).

TABLE 3.2: Relevant observables used in the analysis, labelled by their internal variable names. The events prefixed with `fad` and `ge` are specific for the front AD and MINIBALL events respectively.

Variable	Description
<code>event_t</code>	Time elapsed since the experiment run started.
<code>t1_t</code>	Time of the latest proton pulse at ISOLDE.
<code>ebis_t</code>	Time of the latest EBIS window opening.
<code>fad_sector_id</code>	Index of the sector hit (0 to 3).
<code>fad_ring_number</code>	Index of the ring hit (0 to 23).
<code>fad_strip_number</code>	Index of the strip hit (0 to 15).
<code>fad_ring_e</code>	Energy recorded in ring (calibrated).
<code>fad_strip_e</code>	Energy recorded in strip (calibrated).
<code>ge_clu_id</code>	Index of the cluster hit (0 to 7).
<code>ge_cry_id</code>	Index of the crystal hit (0 to 2).
<code>ge_seg_id</code>	Index of the segment hit (0 to 5).
<code>ge_e</code>	Recorded γ energy (calibrated).

In the next step, the relevant files are calibrated and crudely filtered to discard uninteresting events, after which the files are ready for initial analysis. The C++ software stack that performed the unpacking and calibration is inherited from earlier similar experiments in the collaboration.

The existing analysis programs were not a good fit for the neutron analysis that was the goal of this thesis, which spawned the creation of additional C++ programs to produce a new combined high-level ROOT data structure for the experiment data (see Appendix A.1.1). This final structure was then in turn analysed and visualised via new scripts written in the Python programming language utilising the ROOT Python interface PyROOT, which provides bindings to the C++ core of ROOT (see Appendix A.1.2). This approach was chosen to leverage fast prototyping enabled by using a high-level scripting language for tasks such as histogram building, data export, configuration handling, etc., as compared to the general C++ base of the underlying framework.

3.4.1 Relevant available observables

After the unpacking and calibration steps have been performed, the constructed ROOT tree is processed by the customised analysis program which performs geometrical transformations and possibly event filtering for the task in hand (due to e.g. coincidence criteria and/or energy ranges). Table 3.2 is a reference of the main observables used in the neutron analysis framework.

The sector, strip and ring index for the front AD events can be combined to yield polar

and azimuthal angles as seen from the chamber target to the detector impact point in the laboratory system through known transformations (see Section 3.3.2). Events in the T-REX barrel did not enter into my final analysis, but contain similar information to decide a detector impact point in space. Regarding MINIBALL, the combination of a cluster, crystal and segment is mapped to polar and azimuthal angles through the positional calibration described in Section 3.3.1.

3.4.2 Analysis assumptions

A γ ray in the MINIBALL detector will due to Compton scattering (see Figures 2.3 and 2.4) for a large range of the interesting γ energies in this experiment distribute its total energy between several interactions, whose contributions need to be summed to yield the total energy. The algorithm for γ detection in the existing analysis program suite thus sets the γ event energy to the sum of energies recorded in a certain crystal within a short time interval, and the event position to the point of the first of these recorded energy signals as determined by pulse shape analysis [53]. The neutron detection mechanism suggested in Section 2.4.3, however, will produce a single ejected conversion electron carrying the full identification energy of 690 keV that one should be able to measure directly. Summation of multiple events is thus not needed. The range of this electron within germanium is about 0.3 mm [2], which should make the detection point coincide well with the initial neutron interaction.

The position-sensitive ΔE detectors in T-REX should produce two energy readouts for a single penetrating charged particle as it travels through both the front and back silicon detector layers. To discard non-realistic events, a condition is set where the difference between these energy read-outs needs to stay within 500 keV to be regarded as a true event.

The full data analysis is in general concentrated to energies in the region of 681 keV to 731 keV to account for detector uncertainties and the distribution of added recoil of the ^{72}Ge nucleus hit by the neutron, and also to be able to compare with a small region of background reference at energies below the conversion electron threshold energy. A more drastic selection is made by imposing constraints on the delay between the main target impact and the registered conversion electron, which should help to separate the conversion electrons from γ background coincident with the target collision in itself.

4

Results and analysis

4.1 Improving signal-to-noise ratio

From the full energy spectrum recorded by MINIBALL (see Figure 4.1) the analysis focused on an energy interval around the characteristic neutron-induced ^{72}Ge excitation energy at 690 keV (see Figure 4.2). The “hump” that can be seen in this area already at this stage is assumed to originate from that very process, but the signal-to-noise ratio at about 10 % needs to be improved through different methods.

4.1.1 Backward versus forward angles

Splitting the events detected in the forward and backward directions in MINIBALL from target impact relative to the incoming beam (refer to Figure 3.1) shows that there were in fact more events registered in the backward direction, as seen in Figure 4.3. Expanding the energy spectrum to the full experimental range and selecting events on crystal basis consistently reinforced this observation (see Figure 4.4). The reason is assumed to be noticeable x-ray interference from the accelerating RF cavities in REX-ISOLDE (see Section 2.6.3) due to a known physical process [59, 60], which due to the facility layout is picked up primarily by the backward detectors that in turn shield the forward detectors to some extent. This dependence is further illuminated by comparison with a source run with REX-ISOLDE turned off, where the systematic difference between the forward and backward directions diminishes (see Figure 4.5).

4.1.2 Event timing considerations

Due to the time structure of the beam delivered from REX-ISOLDE, there will not be a uniform distribution of interesting events in time, and there is no reason to expect a uniform SNR during the beam window. By discarding the phases with the lowest discernible peak at 690 keV, overall SNR should be improved.

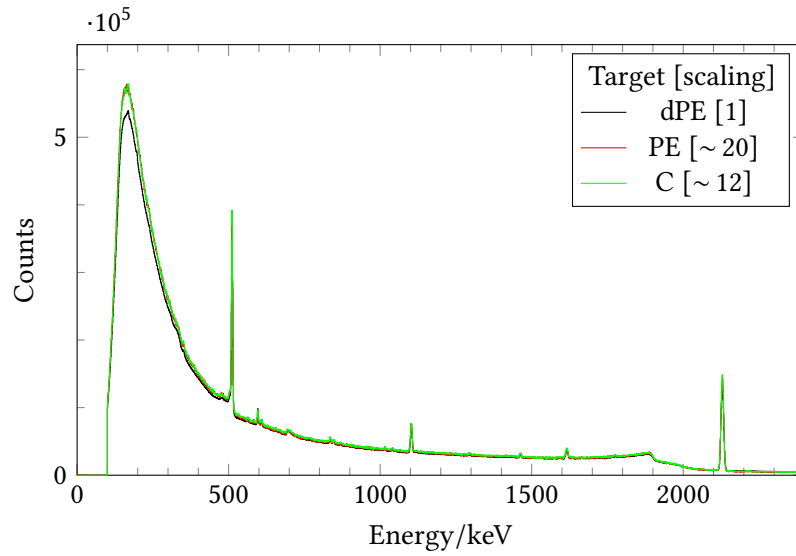


FIGURE 4.1: Full energy spectrum from MINIBALL for different targets. The count rates for the different targets are scaled to similar background levels to be able to visually compare the target runs.

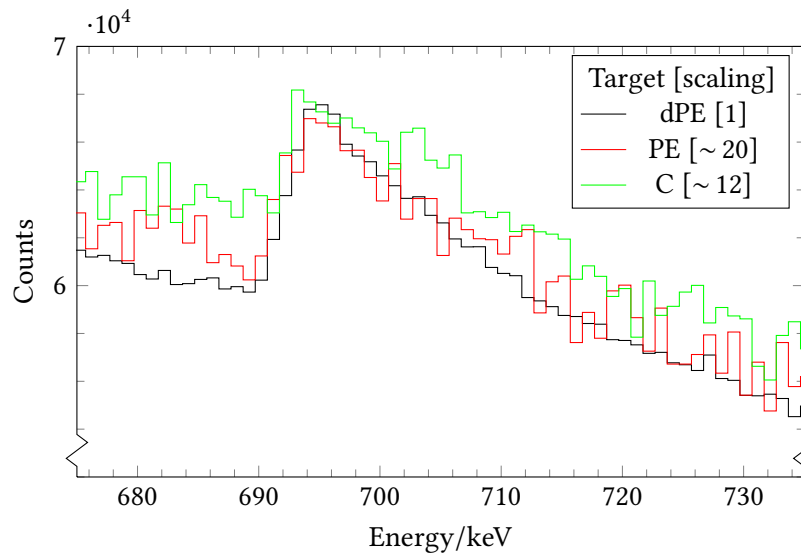


FIGURE 4.2: Energy spectrum from MINIBALL in the region of the characteristic deexcitation energy in ^{72}Ge from the neutron-excited state (see Figure 4.1 for the full spectrum).

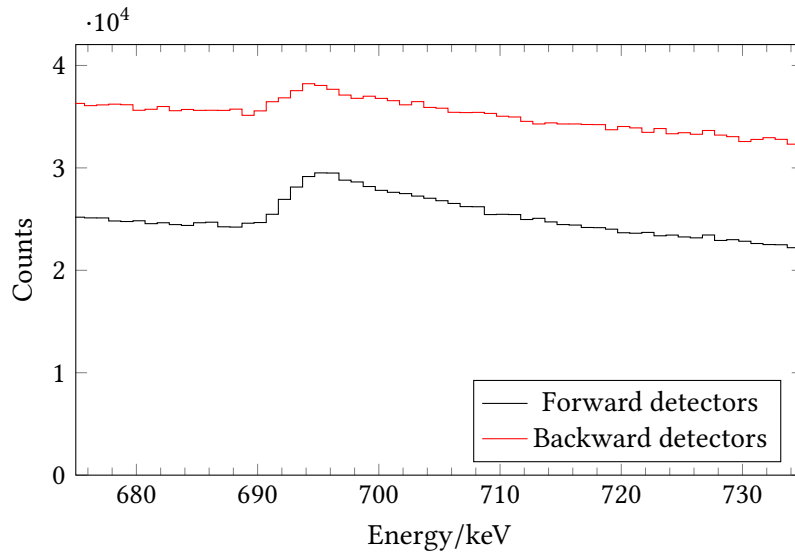


FIGURE 4.3: Energy spectra in MINIBALL split into forward and backward scattering directions from the target impact relative to the incoming beam direction. More events are registered in the backward direction.

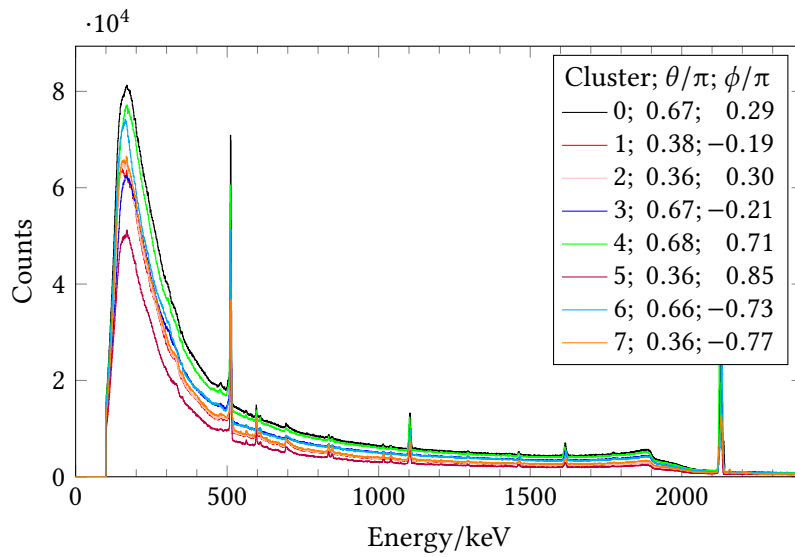


FIGURE 4.4: Wide energy spectrum in MINIBALL split into the separate clusters, denoted by their software index in the range from 0 to 7, with their calibrated polar and azimuthal angles θ and ϕ respectively. Of note is how the backward facing clusters ($\theta > \pi/2$) in general record higher count rates than the ones facing forward.

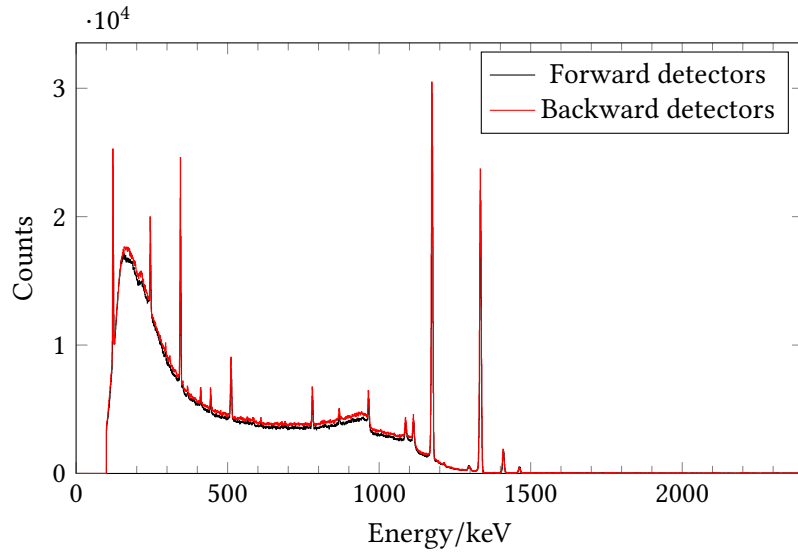


FIGURE 4.5: Energy spectra in MINIBALL split into forward and backward scattering directions from the target impact relative to the incoming beam direction for a source run of ^{60}Co . The count rates are similar with REX-ISOLDE turned off.

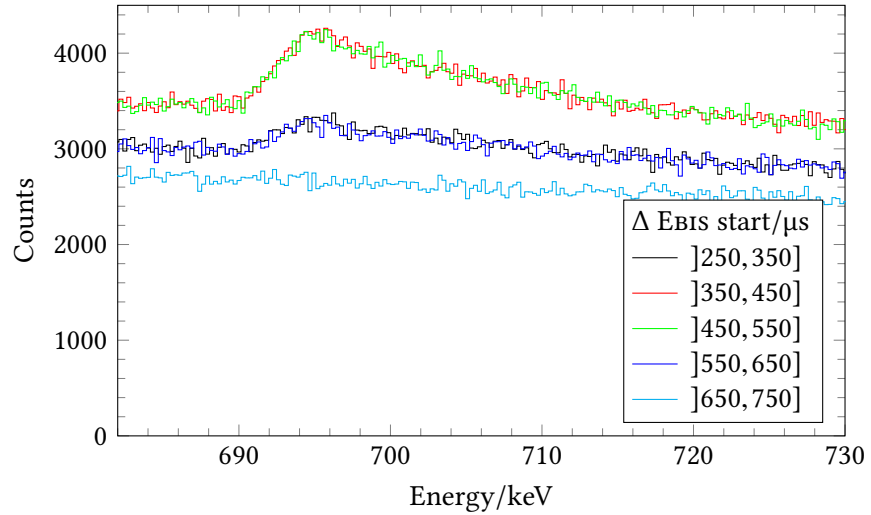


FIGURE 4.6: Sample energy spectra for different time intervals after EBIS window start.

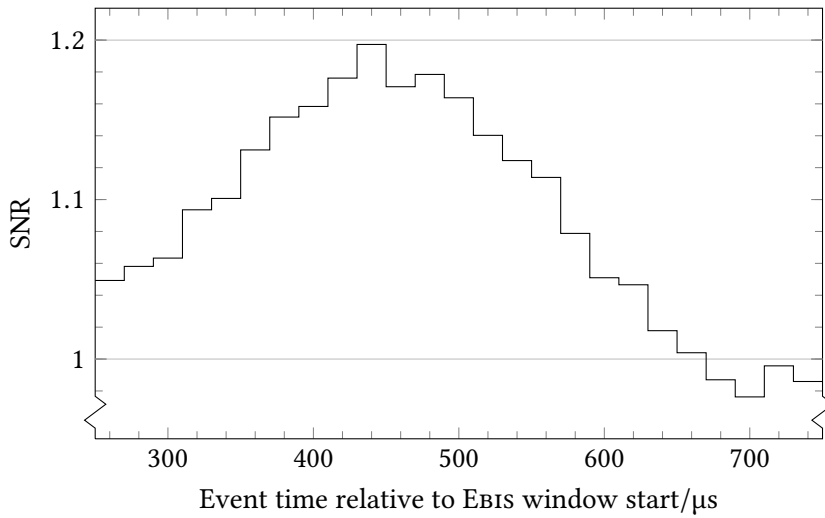


FIGURE 4.7: Signal-to-noise ratio for neutron-like signals versus background at different time intervals after EBIS window start. The histogram shape illustrates that the neutron-like signal raises above the background floor at its highest around $450 \mu\text{s}$ after the opening of the EBIS window.

By selecting events recorded within different time intervals relative to the EBIS window start (see Figure 4.6 for a sample comparison) and comparing the peak-to-background ratio (see Figure 4.7) the most interesting time interval was found around $450 \mu\text{s}$ after the EBIS window start, where it reached a peak-to-background ratio of about 1.2. The “signal” was in this case defined as the integral of the amount of events in an energy region where the peak was visually noticeable, and the “background” was defined as the integral of an equally long energy range situated just below the initial peak.

The timing characteristics of the isotope production stage should not be a factor in this experiment, since the lifetime of the beam isotope ^{11}Be is an order of magnitude larger than the time between proton pulses arriving at ISOLDE. This assumption was tested in a similar fashion to how the SNR dependence on the EBIS time was deduced, and it was found to hold since no clear pattern emerged in the corresponding SNR plot (see Figure 4.8). The more erratic behaviour after about 1 s into the histogram could be explained by the fact that the proton pulses in general arrive at ISOLDE every 1.2 s, but sometimes a proton bunch is skipped, which leads to longer times between the proton pulse and the event within the chamber. As a consequence, a relatively small amount of events are tagged with “ t_1 ” times (defined in Table 3.2) longer than 1.2 s in the experiment as compared to events with t_1 less than 1.2 s, and the more heavily fluctuating SNR values are due to lower statistics.

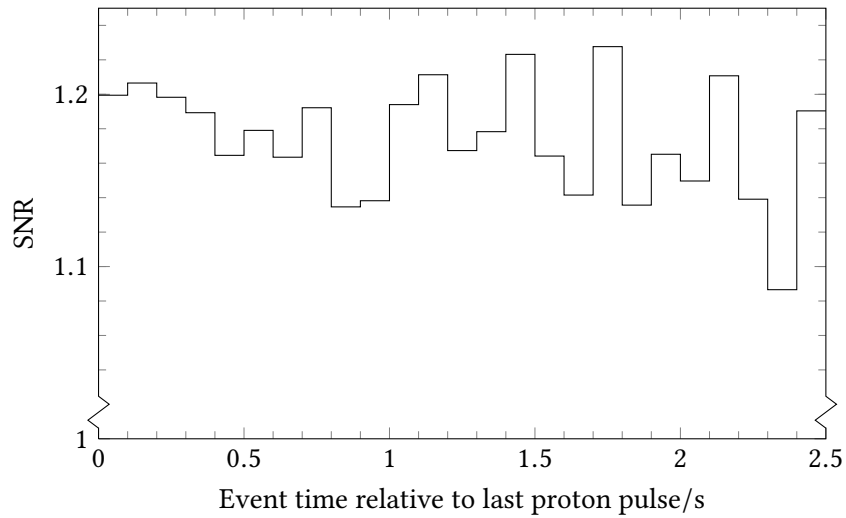


FIGURE 4.8: Signal-to-noise ratio for neutron-like signals versus background at different time intervals after the proton pulse reaches ISOLDE, with a cut on the most favourable times after EBIS window start. The histogram shape shows no discernible pattern, which reinforces the notion that the time structure from the isotope production stage at ISOLDE does not largely affect the time structure of the experiment data, due to the lifetime of the beam isotope in this experiment being an order of magnitude longer than the time between proton pulses.

4.2 Coincidence measurements

4.2.1 Neutron and γ coincidences from the (d,n) reaction

To investigate the $^{11}\text{Be}(d,n)^{12}\text{B}$ reaction, simulations with TALYS [61] were performed to indicate possible coincident γ energies. The idea is to trigger on a characteristic γ energy for the (d,n) reaction registered in MINIBALL and subsequently look for a delayed neutron-like signal, also in MINIBALL. The neutron will pass through T-REX, and the heavy ion will predominantly go to the beam dump, making MINIBALL detection of a neutron an interesting way to find events otherwise experimentally invisible in Is430. However, with the beam energy used in this experiment, the simulations showed that the (d,n) reaction would strongly populate the continuous energy level range in ^{12}B , making it difficult to find a characteristic γ energy indicative of such a reaction for setting the coincidence criterion.

4.2.2 Neutron and ion coincidences from the (d,n) reaction

Instead, focus was turned to find events in coincidence with the detection of the heavy ion in T-REX. With the experiment setup and energies, combined with the Q values for the reaction, detection of the heavy fragment becomes a rare event. No heavy fragments

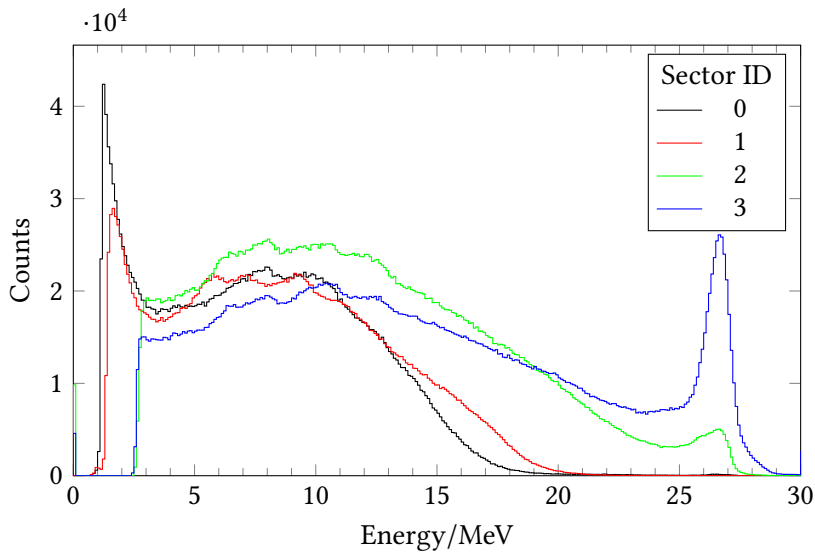


FIGURE 4.9: Energy loss spectrum in the strips for the individual sectors of the front AD. Note that the right edges of sector index 2 and 3 include a rising peak from non-penetrating energetic events, while these are not present for index 0 and 1 due to gain settings.

are picked up in the backward barrel due to kinematics. The forward barrel was shielded with a foil during this experiment for the very purpose of keeping heavy fragments from hitting the detector (see Section 3.2.2). The front AD only covers polar laboratory angles down to 8° , and the thickness of the ΔE detectors fully stops the heavy ions, removing the possibility to distinguish ^{12}B from e.g. ^{11}Be based on telescope considerations alone.

A further issue is that only two of the four sectors of the front AD registered events from heavy non-penetrating ejectiles (see Figure 4.9) due to differing signal gain settings for the sectors, mainly adjusted to detect the light particles with as much granularity as possible, since those were the main focus of the experiment. Another possible explanation for the different maximum detected energies of the sectors could have been that the front AD was not properly centred around the beam, making it less probable for heavy ions to deflect enough in the laboratory system to reach certain sectors. The beam centring had already been investigated by Johansen and was found to be radially shifted 1.3 mm as compared to an ideally centred beam line [46, Section 6.3]. Looking at the angular distribution of the high-energy events in the ΔE detectors shows that even though the events as expected are mainly present at small angles, the angular spread is large enough for at least some events to hit every sector even if the beam centring were to be off by the order of mm, so this should not be a large factor in explaining the difference in the energy spectra for the different sectors.

Consequences of this includes:

1. The useful statistics will be lowered. One could tag overflow events as heavy-ion hits, but the exact energy would in any case be lost, which is important to be able to extract interesting excitation energies through angular relations.
2. The lower energy edge of the non-penetrating events is seen in Figure 4.9 to be around 25 MeV, which is at best cut off at about 28 MeV. The (d,n) reaction is exothermic at $Q = 11.87$ MeV, which together with the beam energy of 31.35 MeV (see Section 3.1.1) when evaluating Equation (2.7) yields an interesting ion energy region that largely falls outside of the detector range at the observed angles (the kinematic curve is later shown in Figure 4.13).

A further factor to note is the lifetime of the neutron-induced state in ^{72}Ge which smears the coincidence criterion in time, with two immediate consequences:

1. The identification of an actual coincidence needs to be generous in the timing condition, possibly including false coincidences.
2. The substantial background from the deexcitation of various excited states in the nucleus can be avoided by selecting coincidence events timewise separated from the prompt γ cascade at impact.

The second point is illustrated in Figure 4.10, where one can note the horizontal lines at 511 keV, 690 keV and 2100 keV which correspond to events spread out in time. These lines are assumed to originate mainly from an E0 transition in ^{12}Be leading to $e^- + e^+$ annihilation,* the long-lived ^{72}Ge state (which is of interest here) and the β^- decay $^{11}\text{Be} \rightarrow ^{11}\text{B}$ respectively [46, Section 7.2.3.2].

*This annihilation process produces two 511 keV γ in opposite directions. The positrons originate from background β^+ decays.

A further observation in Figure 4.10 is how the γ background within this experiment largely resides within 100 ns after ion detection, further illustrated in Figure 4.11, while the mean lifetime of the neutron-induced state in ^{72}Ge is $\tau = 444.2(8)$ ns. Cutting away $t = 100$ ns after ion detection should thus leave $\exp(-t/\tau) = 80\%$ of the neutron-induced events while removing a large portion of γ background.

Also noteworthy in Figure 4.11 is the low count rate for these coincidences. It would be quite a stretch to find the characteristic exponential decay curve in the time spectrum.

Further investigating the coincidences by separating the prompt and the delayed events to look at their respective angular distribution in Figure 4.12 lends further credibility to the notion that the delayed events in fact are random coincidences with γ background. The prompt events are inching towards spherical symmetry, while the profile of the delayed events is similar to the ones seen earlier of pure background events in the energy interval around the neutron-induced state.

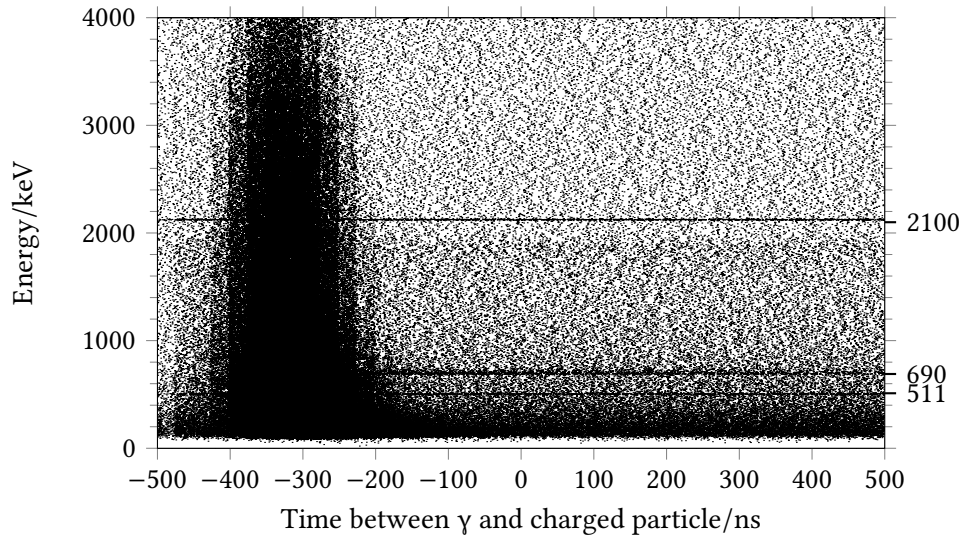


FIGURE 4.10: Energy of γ versus time difference between detection of a charged particle and a γ signal. The large body of events are deduced to be simultaneous events in relation to the observed timescale. The offset of about 300 ns is assumed to be due to differences in readout times between T-REX and MINIBALL. Horizontal lines correspond to events spread out in time, where the 690 keV in particular is assumed to indicate neutron interactions within the crystals.

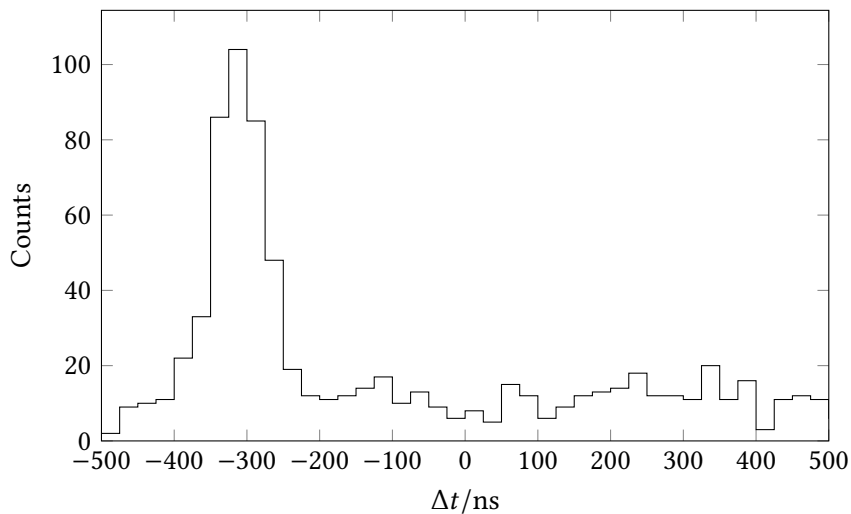


FIGURE 4.11: Time difference between detection of a heavy charged particle in T-REX and a 681 keV to 721 keV signal in MINIBALL. The large amount of events around -300 ns indicate the reaction time offset as described in Figure 4.10. The events spread towards the right of the main peak should contain $^{72}\text{Ge}^*$ deexcitations with the time profile of the neutron-induced state. The statistics are poor, and no clear exponential decay for the delayed events is found.

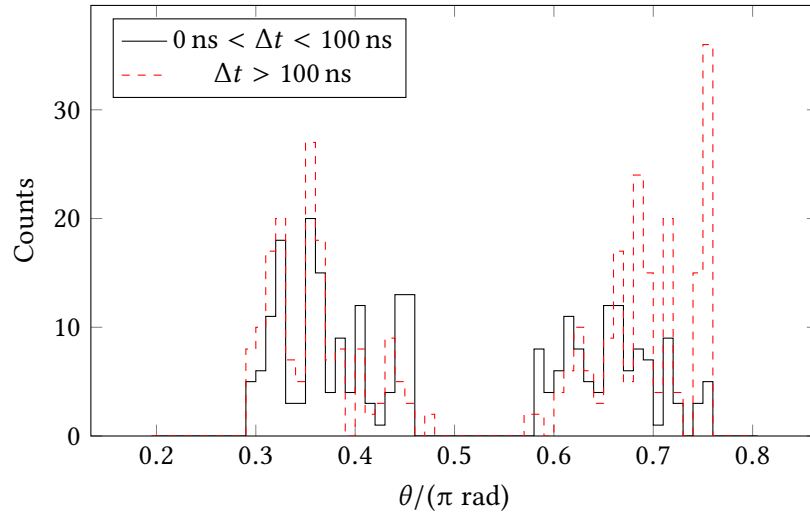


FIGURE 4.12: Polar angle distributions for coincidence events between heavy ions and neutrons, separated on the delay from the assumed impact time. The times have been compensated for the readout offset noted in Figure 4.11. The events with a delay of more than 100 ns are seen to predominantly register at large polar angles, which corresponds to the general γ background in the experiment. Note that the histogram structure also reflects the non-uniform angular coverage of MINIBALL in the experiment (see Figure 3.2).

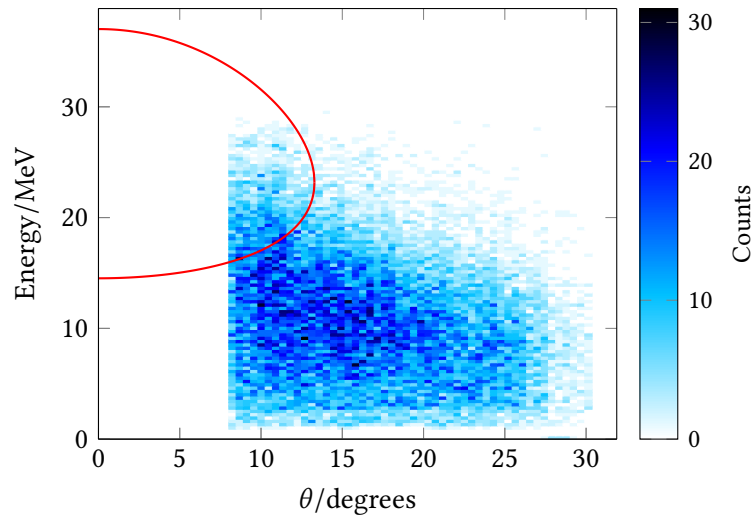


FIGURE 4.13: Relation between energy and polar angle for charged particle events in the front AD in coincidence with a neutron-like signal in MINIBALL, compared with the theoretical kinematic curve from Equation (2.7) for the (d,n) process, assuming population of the ground state in ^{12}B as per the reasoning in the text.

The spectrum in Figure 4.12 should be compared to the non-symmetric polar angular placement of the recording segments of MINIBALL shown in Figure 3.2.

The angle and energy of signals in the front AD detected in coincidence with a neutron-like signal in MINIBALL were plotted in a histogram overlaid with the expected kinematic curves for the (d,n) reaction as per the relation in Equation (2.7) (see Figure 4.13). The single curve shown assumes that the ground state of ^{12}B is populated, i.e. $E_{\text{ex}} = 0$ in Equation (2.8), with the rationale that the effect of a non-zero realistic E_{ex} is negligible due to the high Q value for the reaction. There is no conclusive correlation seen between the kinematic curve and the energy and angle data of charged particles detected in coincidence with neutron-like signals in MINIBALL, and the statistics for this channel are poor, in line with the earlier reasoning about the energy and angular range of the front AD.

This page intentionally contains only this sentence.

5

Summary

A mechanism for detecting neutrons in the germanium-based MINIBALL detector array via a specific deexcitation in ^{72}Ge resulting from inelastic neutron scattering was investigated using data from experiment Is430. New programs for data analysis of T-REX and MINIBALL data were written to encompass event selection on neutron-like energy signals in MINIBALL and to make graph creation more versatile and efficient for the task in hand. The graphs produced were analysed to gain insights on the extent to which the experimental neutron detection mechanism could be of use in this and other similar experiments with MINIBALL and other germanium detector configurations.

5.1 Conclusions

Signals at the expected neutron-induced γ energies were clearly visible among the data with a time profile stretched from the prompt reaction as expected due to the lifetime of the first excited state in ^{72}Ge . However, due to the combination of the physical processes involved and the experiment parameters, some vital information to enable deeper nuclear study was found missing.

A known energy-dependence of the cross section of neutrons on ^{72}Ge would have been needed to perform useful simulations to compare with the experiment. Such cross section data was not found to be available at the time.

The possibility to put a coincidence criterion on the detection of a neutron-like signal and a characteristic known γ deexcitation from a (d,n) reaction was obstructed due to the beam energy being sufficiently high to populate the continuous energy spectrum in the resulting nucleus.

The detection of a heavy charged fragment was in general a rare event in the experiment configuration. In the front AD, the detector gain was calibrated to give maximum resolution for the light charged ejectiles that were the main concern of the primary experiment. A consequence of this was that heavy ion interactions in the interesting range for

the (d,n) channel were collected in the overflow bin without recording the exact energies that would be useful for this analysis. The forward barrel section of the detector which covered angles larger than the front AD was shielded with a foil with the exact purpose of stopping heavy ions from reaching the detector stage.

The tentative neutron coincidence measurements performed by Johansen in his thesis were hampered in part by the problem of unrelated background excitations from carbon fusion being close in energy to the potentially interesting neutron-like signals [46, Section 10.3.2]. This coupled to the problem of too low statistics being available after coincidence restraints had been applied, and no clear patterns discernible from background noise emerged from the attempts.

Coincidence measurements are deemed necessary to extract useful information from the γ energy spectrum due to the prevalence of a broad x-ray background from the experiment conditions, not least in combination with the non-symmetric effects found where the detectors closer to the accelerating component of the experiment absorbed a larger portion of the RF cavity radiation.

The main focus of experiment Is430 was to investigate the structure and states of ^{10}Be , ^{11}Be and ^{12}Be through transfer reactions, using ^{11}Be as an exotic radioactive beam and an experiment configuration aimed at simultaneous charged particle and γ detection. As a consequence, the experiment parameters were not optimally tuned to enable neutron detection through MINIBALL, and the investigation of the feasibility of the method was rather motivated by an experimental curiosity in this context, uncovering several shortcomings during the analysis. The scientific benefit of the analysis performed lies primarily in formulating the problems encountered to enable future preparatory investigations to draw from this knowledge to better predict how and when the method can be of use in an experiment context.

5.2 Outlook

Perhaps the most pressing matter for future enhancements of experiment analysis using the neutron detection method described in this thesis would be to obtain data on the energy dependent cross section of inelastic neutron scattering on ^{72}Ge needed for simulations. With the prevalence of germanium-based detectors, such a measurement does not seem to be unreasonable to justify, e.g. to enable using the side-band neutron detection channel as an online diagnostic tool to measure the neutron incidence rate on the crystals.

To further investigate or use this method in future experiments in the context of nuclear physics, consideration of the unfortunate parameters described in Section 5.1 should be included as a part of the preparatory work to avoid situations where the channels that could benefit from neutron data are out of reach for the detection mechanisms used. Such

a consideration would also benefit from the possibility to perform accurate simulations in order to investigate the impact of the parameter choices in the planning stage.

This page intentionally contains only this sentence.

List of Figures

1.1	Half-life of known isotopes.	5
1.2	Illustration of the halo structure of ^{11}Be	7
1.3	Map of CERN members as of 2014.	7
2.1	Illustration of the impact parameter and scattering angle during a nuclear scattering process.	13
2.2	Illustration of the $^{11}\text{Be}(d, t)^{10}\text{Be}$ transfer reaction in direct kinematics.	13
2.3	Qualitative scheme over the dominant regions for the different matter interaction processes for photons depending on photon energy E_γ and proton number Z of the detector material.	19
2.4	Illustrations of matter interaction processes for photons.	19
2.5	Scheme of the low-lying energy levels of ^{72}Ge	21
2.6	Schematic of the ISOLDE hall in general and REX-ISOLDE in particular.	24
3.1	Cutaway rendering of the T-REX and MINIBALL configuration.	32
3.2	Polar angle distribution of segments in MINIBALL.	34
4.1	Full energy spectrum from MINIBALL for different targets.	38
4.2	Energy spectrum from MINIBALL in the region of the characteristic deexcitation energy in ^{72}Ge from the neutron-excited state.	38
4.3	Energy spectra in MINIBALL split into forward and backward scattering directions from the target impact relative to the incoming beam direction.	39
4.4	Wide energy spectrum in MINIBALL split into the separate clusters.	39
4.5	Energy spectra in MINIBALL split into forward and backward scattering directions from the target impact relative to the incoming beam direction for a source run of ^{60}Co	40
4.6	Sample energy spectra for different time intervals after EBIS window start.	40
4.7	SNR for neutron-like signals versus background at different time intervals after EBIS window start.	41
4.8	SNR for neutron-like signals versus background at different time intervals after the proton pulse, selected on the most favourable times after EBIS window start.	42
4.9	Energy loss spectrum in the strips for the individual sectors of the front AD.	43
4.10	Energy of γ versus time difference between detection of a charged particle and a γ signal.	45
4.11	Time difference between detection of a heavy charged particle in T-REX and a 681 keV to 721 keV signal in MINIBALL.	45

- 4.12 Polar angle distributions for coincidence events between heavy ions and neutrons, separated on the delay from the assumed impact time. 46
- 4.13 E - θ relation for charged particle events in the front AD in coincidence with a neutron-like signal in MINIBALL. 46

References

- [1] C. Chasman, K. Jones, and R. Ristinen. Fast neutron bombardment of a lithium-drifted germanium gamma-ray detector. *Nucl. Instrum. Methods* **37** (Nov. 1965), 1–8. DOI: 10.1016/0029-554X(65)90328-9. Cited on page 2.
- [2] D. Jenkins et al. Proof-of-principle for fast neutron detection with advanced tracking arrays of highly segmented germanium detectors. *Nucl. Instrum. Methods Phys. Res., Sect. A* **602.2** (Apr. 2009), 457–460. ISSN: 0168-9002. DOI: 10.1016/j.nima.2009.01.171. Cited on pages 2, 20, 36.
- [3] K. S. Krane. *Introductory nuclear physics*. John Wiley & Sons, 1987. ISBN: 047180553X. Cited on pages 3, 6, 11, 16–17, 22, 25.
- [4] Nobelprize.org. *The Nobel prize in Physics 1963*. Nobel Media AB. URL: http://www.nobelprize.org/nobel_prizes/physics/laureates/1963/, visited on 2014-08-27. Cited on page 3.
- [5] J. Erler et al. The limits of the nuclear landscape. *Nature* **486.7404** (June 2012), 509–512. ISSN: 1476-4687. DOI: 10.1038/nature11188. Cited on page 4.
- [6] C. Thibault et al. Direct measurement of the masses of ^{11}Li and $^{26-32}\text{Na}$ with an on-line mass spectrometer. *Phys. Rev. C* **12.2** (Aug. 1975), 644–657. ISSN: 0556-2813. DOI: 10.1103/physrevc.12.644. Cited on page 4.
- [7] B. Wildenthal and W. Chung. Collapse of the conventional shell-model ordering in the very-neutron-rich isotopes of Na and Mg. *Phys. Rev. C* **22.5** (Nov. 1980), 2260–2262. ISSN: 0556-2813. DOI: 10.1103/physrevc.22.2260. Cited on page 4.
- [8] A. Navin et al. Direct evidence for the breakdown of the $N = 8$ shell closure in ^{12}Be . *Physical Review Letters* **85.2** (July 2000), 266–269. ISSN: 1079-7114. DOI: 10.1103/physrevlett.85.266. Cited on page 4.
- [9] O. Sorlin and M.-G. Porquet. Nuclear magic numbers: New features far from stability. *Prog. Part. Nucl. Phys.* **61.2** (Oct. 2008), 602–673. DOI: 10.1016/j.pnpnp.2008.05.001. Cited on page 4.
- [10] J. K. Tuli, ed. *Nuclear wallet cards*. Brookhaven National Laboratory, June 1, 2012. URL: <http://www.nndc.bnl.gov/wallet/>, visited on 2014-09-08. Cited on pages 5, 22.
- [11] L. Hafstad and E. Teller. The alpha-particle model of the nucleus. *Phys. Rev.* **54.9** (Nov. 1938), 681–692. ISSN: 1536-6065. DOI: 10.1103/physrev.54.681. Cited on page 6.
- [12] A. Arima et al. Clustering in light nuclei. *Adv. Nucl. Phys.* (1972), 345–477. DOI: 10.1007/978-1-4615-8231-1_3. Cited on page 6.

- [13] M. Freer. The clustered nucleus — cluster structures in stable and unstable nuclei. *Rep. Prog. Phys.* **70.12** (Dec. 2007), 2149–2210. ISSN: 1361-6633. DOI: 10.1088/0034-4885/70/12/r03. Cited on page 6.
- [14] W. von Oertzen. Two-center molecular states in ${}^9\text{B}$, ${}^9\text{Be}$, ${}^{10}\text{Be}$, and ${}^{10}\text{B}$. *Z. Phys. A: Hadrons Nucl.* **354.1** (Dec. 1996), 37–43. ISSN: 0939-7922. DOI: 10.1007/s002180050010. Cited on page 6.
- [15] P. G. Hansen and B. Jonson. The neutron halo of extremely neutron-rich nuclei. *Europhys. Lett.* **4.4** (Aug. 1987), 409–414. DOI: 10.1209/0295-5075/4/4/005. Cited on pages 6, 9.
- [16] T. Nilsson, G. Nyman, and K. Riisager. Halo-nuclei at ISOLDE. *Hyperfine Interact.* **129.1/4** (2000), 67–81. ISSN: 0304-3834. DOI: 10.1023/a:1012678320350. Cited on pages 6, 29.
- [17] CERN. *Member states*. 2014. URL: <http://home.web.cern.ch/about/member-states>, visited on 2014-08-21. Cited on pages 6–7.
- [18] *CERN member countries on map of Europe*. Licensed under CC BY-SA 3.0 (<http://creativecommons.org/licenses/by-sa/3.0/deed.en>). URL: http://en.wikipedia.org/wiki/File:Location_CERN_member_countries_on_map_of_Europe.svg, visited on 2014-08-21. Cited on page 7.
- [19] CERN. *International Relations: Sweden*. 2014. URL: <http://international-relations.web.cern.ch/international-relations/ms/se.html>, visited on 2014-08-25. Cited on page 6.
- [20] CERN. *Member states' contributions 2014*. URL: <http://dg-rpc.web.cern.ch/dg-rpc/Scale/MemberStatesContributions2014.html>, visited on 2014-08-25. Cited on page 6.
- [21] F. Combley, F. Farley, and E. Picasso. The CERN muon ($g-2$) experiments. *Phys. Rep.* **68.2** (1981), 93–119. ISSN: 0370-1573. DOI: 10.1016/0370-1573(81)90028-4. Cited on page 8.
- [22] G. Arnison et al. Experimental observation of isolated large transverse energy electrons with associated missing energy at $s = 540$ GeV. *Phys. Lett. B* **122.1** (1983), 103–116. ISSN: 0370-2693. DOI: 10.1016/0370-2693(83)91177-2. Cited on page 8.
- [23] G. Arnison et al. Experimental observation of lepton pairs of invariant mass around $95 \text{ GeV}/c^2$ at the CERN SPS collider. *Phys. Lett. B* **126.5** (1983), 398–410. ISSN: 0370-2693. DOI: 10.1016/0370-2693(83)90188-0. Cited on page 8.
- [24] Nobelprize.org. *The Nobel prize in Physics 1984*. Nobel Media AB. URL: http://www.nobelprize.org/nobel_prizes/physics/laureates/1984/, visited on 2014-08-25. Cited on page 8.
- [25] G. Taubes. *Nobel dreams: Power, deceit, and the ultimate experiment*. Random House, New York, 1986. ISBN: 9780394545035. Cited on page 8.

- [26] CERN. *New state of matter created at CERN*. Feb. 10, 2000. URL: <http://press.web.cern.ch/press-releases/2000/02/new-state-matter-created-cern>, visited on 2014-08-26. Cited on page 8.
- [27] CERN. *Heavy ions and quark-gluon plasma*. URL: <http://home.web.cern.ch/about/physics/heavy-ions-and-quark-gluon-plasma>, visited on 2014-08-26. Cited on page 8.
- [28] CERN press release. *CERN experiments observe particle consistent with long-sought Higgs boson*. July 4, 2012. URL: <http://press.web.cern.ch/press-releases/2012/07/cern-experiments-observe-particle-consistent-long-sought-higgs-boson>, visited on 2014-08-26. Cited on page 8.
- [29] CERN. *New results indicate that new particle is a Higgs boson*. Mar. 14, 2013. URL: <http://home.web.cern.ch/about/updates/2013/03/new-results-indicate-new-particle-higgs-boson>, visited on 2014-08-26. Cited on page 8.
- [30] Nobelprize.org. *The Nobel prize in Physics 2013*. Nobel Media AB. URL: http://www.nobelprize.org/nobel_prizes/physics/laureates/2013/, visited on 2014-08-26. Cited on page 8.
- [31] B. Jonson and A. Richter. More than three decades of ISOLDE physics. *Hyperfine Interact.* **129**.1–4 (2000), 1–22. ISSN: 0304-3843. DOI: 10.1023/A:1012689128103. Cited on page 9.
- [32] J. Äystö. CERN's longest serving experimental facility. *Phys. Rep.* **403–404** (Dec. 2004), 459–469. ISSN: 0370-1573. DOI: 10.1016/j.physrep.2004.08.030. Cited on page 9.
- [33] Chalmers University of Technology. *Chalmers → Fundamental physics → Research groups → Subatomic physics*. Apr. 3, 2012. URL: <http://www.chalmers.se/fp/EN/research/research-groups/subatomic-physics>, visited on 2014-08-26. Cited on page 9.
- [34] E. M. Henley and A. Garcia. *Subatomic physics*. 3rd ed. World Scientific Publishing Company, 2007. ISBN: 978-981-270-056-8. Cited on page 11.
- [35] W. R. Leo. *Techniques for nuclear and particle physics experiments: A how-to approach*. 2nd ed. Springer, 1994. ISBN: 3540572805. Cited on pages 11, 25.
- [36] W. M. Stacey. *Nuclear reactor physics*. 1st ed. John Wiley & Sons, 2001. ISBN: 0471391271. Cited on page 20.
- [37] G. Braun, A. Bockisch, and W. Neuwirth. Lifetime of the 0_2^+ state of ^{72}Ge determined by delayed auto-coincidence of a Ge(Li) detector. *Nucl. Instrum. Methods Phys. Res.* **224**.1–2 (July 1984), 112–116. DOI: 10.1016/0167-5087(84)90454-X. Cited on page 20.
- [38] S. Ilieva. “Investigation of the nuclear matter density distributions of the exotic ^{12}Be , ^{14}Be and ^8B nuclei by elastic proton scattering in inverse kinematics”.

- PhD thesis. Fachbereich Physik, Johannes Gutenberg-Universität, 2008. URN: nbn:de:hebis:77-18903 . Cited on page 21.
- [39] M. Lindroos. Future plans at ISOLDE. *Nucl. Instrum. Methods Phys. Res., Sect. B* **204** (May 2003), 730–735. ISSN: 0168-583X. DOI: 10.1016/s0168-583x(03)00494-4. Cited on page 22.
- [40] E. Kugler. The ISOLDE facility. *Hyperfine Interact.* **129.1/4** (2000), 23–42. ISSN: 0304-3834. DOI: 10.1023/a:1012603025802. Cited on page 22.
- [41] D. Habs et al. The REX-ISOLDE project. *Hyperfine Interact.* **129.1/4** (2000), 43–66. ISSN: 0304-3834. DOI: 10.1023/a:1012650908964. Cited on pages 22–23.
- [42] D. Habs et al. “The q/m -separator for REX-ISOLDE”. (6th European Particle Accelerator Conference, June 22–26, 1998). Stockholm, Sweden, 1998. URL: <http://cds.cern.ch/record/859316/>. Cited on page 25.
- [43] M. Lindroos et al. HIE-ISOLDE. *Nucl. Instrum. Methods Phys. Res., Sect. B* **266.19–20** (Oct. 2008), 4687–4691. DOI: 10.1016/j.nimb.2008.05.136. Cited on page 25.
- [44] CERN. *The HIE-ISOLDE project*. URL: <https://hie-isolde.web.cern.ch/hie-isolde/>, visited on 2014-05-06. Cited on page 25.
- [45] L. Grassi et al. Study of DSSSD detector response in the inter-strip region using a proton micro-beam. *EPJ Web of Conferences* **66.11015** (2014). Ed. by S. Lunardi et al. ISSN: 2100-014X. DOI: 10.1051/epjconf/20146611015. Cited on page 27.
- [46] J. G. Johansen. “Transfer reaction study of neutron rich beryllium isotopes”. Presented 2012. PhD thesis. Department of Physics and Astronomy, Aarhus University, 2012. URL: <https://cds.cern.ch/record/1529675/>. Cited on pages 29–31, 33–34, 43–44, 50.
- [47] J. Lettry et al. Pulse shape of the ISOLDE radioactive ion beams. *Nucl. Instrum. Methods Phys. Res., Sect. B* **126.1–4** (Apr. 1997), 130–134. ISSN: 0168-583X. DOI: 10.1016/s0168-583x(96)01025-7. Cited on page 29.
- [48] V. Bildstein et al. T-REX: a new setup for transfer reaction experiments at REX-ISOLDE. *Eur. Phys. J. A* **48.6** (June 2012). ISSN: 1434-601X. DOI: 10.1140/epja/i2012-12085-6. Cited on pages 31–32.
- [49] H.-H. Boie. “Bremsstrahlung emission probability in the α decay of ^{210}Po ”. Presented 2009. PhD thesis. Combined Faculties for the Natural Sciences and for Mathematics, Ruperto-Carola University of Heidelberg, 2009. URN: nbn:de:bsz:16-heidok-95359 . Cited on page 32.
- [50] S. Agostinelli et al. Geant4 – a simulation toolkit. *Nucl. Instrum. Methods Phys. Res., Sect. A* **506.3** (July 2003), 250–303. ISSN: 0168-9002. DOI: 10.1016/s0168-9002(03)01368-8. Cited on page 32.
- [51] J. Allison et al. Geant4 developments and applications. *IEEE Trans. Nucl. Sci.* **53.1** (Feb. 2006), 270–278. ISSN: 0018-9499. DOI: 10.1109/tns.2006.869826. Cited on

- page 32.
- [52] K. Wimmer. “Discovery of the shape coexisting 0^+ state in ^{32}Mg ”. Presented 2010. PhD thesis. Physik-Department E12, Technische Universität München, 2010. URN: nbn:de:bvb:91-diss-20100819-982690-1-3 . Cited on pages 32–33.
 - [53] N. Warr et al. The MINIBALL spectrometer. *Eur. Phys. J. A* **49.3** (Mar. 2013). ISSN: 1434-601X. DOI: 10.1140/epja/i2013-13040-9. Cited on pages 31, 36.
 - [54] J. Eberth et al. MINIBALL: a gamma-ray spectrometer with position-sensitive Ge detectors for nuclear structure studies at REX-ISOLDE. *AIP Conference Proceedings* **656.1** (2003), 349–356. DOI: 10.1063/1.1556664. Cited on page 31.
 - [55] R. Lutter et al. MAR_aB₀U: a MBS and ROOT based online/offline utility. *IEEE Trans. Nucl. Sci.* **47.2** (Apr. 2000), 280–283. ISSN: 0018-9499. DOI: 10.1109/23.846164. Cited on page 34.
 - [56] H. Essel and N. Kurz. The general purpose data acquisition system MBS. *IEEE Trans. Nucl. Sci.* **47.2** (Apr. 2000), 337–339. ISSN: 0018-9499. DOI: 10.1109/23.846176. Cited on page 34.
 - [57] R. Brun and F. Rademakers. ROOT – An object oriented data analysis framework. *Nucl. Instrum. Methods Phys. Res., Sect. A* **389.1–2** (Apr. 1997), 81–86. ISSN: 0168-9002. DOI: 10.1016/S0168-9002(97)00048-X. Cited on page 34.
 - [58] R. Lutter. *MED data structure*. GSI. 2005. URL: <http://www.bl.physik.uni-muenchen.de/marabou/html/doc/doc/MedStructure.pdf>, visited on 2014-09-17. Cited on page 34.
 - [59] M. Silari et al. Radiation produced by the LEP superconducting RF cavities. *Nucl. Instrum. Methods Phys. Res., Sect. A* **432.1** (Aug. 1999), 1–13. ISSN: 0168-9002. DOI: 10.1016/S0168-9002(99)00455-6. Cited on page 37.
 - [60] O. Kester et al. Accelerated radioactive beams from REX-ISOLDE. *Nucl. Instrum. Methods Phys. Res., Sect. B* **204** (May 2003), 20–30. ISSN: 0168-583X. DOI: 10.1016/S0168-583X(02)01886-4. Cited on page 37.
 - [61] A. Koning, S. Hilaire, and M. Duijvestijn. “TALYS-1.0”. *Proceedings of the International Conference on Nuclear Data for Science and Technology – ND2007*. (Nice, France, Apr. 22–26, 2007). Ed. by O. Bersillon et al. EDP Sciences, 2008, pp. 211–214. DOI: 10.1051/ndata:07767. Cited on page 42.

This page intentionally contains only this sentence.

A

Appendix

A.1 Code samples

A large portion of the project time was spent writing and reading source code. Some illustrative examples of written code are included below. Apart from what is presented here, there were several shell scripts written for automation purposes, and even AWK* got involved in the analysis at times.

*A standard Unix tool and language mainly aimed at efficient text processing, but it can also be (ab)used for different tasks.

I made heavy use of version control systems during the work; the lack of which among the existing code base was a bit surprising. Discussions during our group meetings seemed to indicate a current tendency within the field to gradually embrace such technologies for current and future projects, though.

The programs primarily ran on different branches of the Debian GNU/Linux operating system, but should be portable. Parts of the analysis suites were known to also run successfully on Scientific Linux, Ubuntu and OS X.

A.1.1 Intermediate tree creation

Sample C++ code for creating selective intermediate ROOT trees for histogram creation as mentioned in Section 3.4 is included below. The particular example program listed selects every event in the front AD of T-REX (see Section 3.2.2) in coincidence with a neutron-like signal in MINIBALL, using the ROOT libraries to read the input trees and create a new output tree, which in turn could be analysed further. Common functions used in several similar programs for different event selection criteria were put in the external LibNeutrons.cc/LibNeutrons.hh files, also included below.

```
1  /** FADAndNeutrons.cc
2  * FADAndNeutrons.cc
3  *
4  * Produce intermediate ROOT trees from IS430 experiment data, selecting front
5  * AD events in T-Rex in coincidence with neutron-like signals in Miniball.
```

```

6  */
7
8  #include <cstdlib>
9  #include <iomanip>
10 #include <iostream>
11
12 #include <TChain.h>
13 #include <TFile.h>
14 #include <TTree.h>
15
16 #include "Annular.hh"
17 #include "CommandLineInterface.hh"
18 #include "Germanium.hh"
19 #include "LibNeutrons.hh"
20
21 using std::cerr;
22 using std::cout;
23 using std::endl;
24 using std::flush;
25
26 ClassImp(Annular);
27 ClassImp(Germanium);
28
29 int main(int argc, char **argv)
30 {
31     // CLI argument parsing.
32     std::vector<char*> input_files;
33     char *output_file = NULL;
34     char *mb_angles_file = NULL;
35     bool verbose = false;
36
37     CommandLineInterface interface;
38     interface.Add((char*)"-i", (char*)"input files", &input_files);
39     interface.Add((char*)"-o", (char*)"output file", &output_file);
40     interface.Add((char*)"-M", (char*)"miniball angle", &mb_angles_file);
41     interface.Add((char*)"-v", (char*)"verbose", &verbose);
42     interface.CheckFlags(argc, argv);
43     if (0 == input_files.size() || 0 == output_file) {
44         cerr << "You have to provide at least one input file and the output file!"
45              << endl;
46         return ExitStatus::IO_MISSING;
47     }
48
49     // Status printout.
50     cout << "Input file(s):" << endl;
51     for (size_t i = 0; i < input_files.size(); ++i) {
52         cout << " " << input_files[i] << endl;
53     }
54     cout << "Output file: " << output_file << endl;
55
56     // Combine input file data to single ROOT structure.
57     TChain in_chain("caltr");
58     for (size_t i = 0; i < input_files.size(); ++i) {
59         in_chain.Add(input_files[i]);
60     }

```

```

61
62  if (0 == in_chain.GetEntries()) {
63      cout << "Could not find tree 'caltr' in files:" << endl;
64      for (size_t i = 0; i < input_files.size(); ++i) {
65          cout << " " << input_files[i] << endl;
66      }
67      return ExitStatus::NO_CALTR;
68  }
69
70  // Initiate and populate Miniball angle data.
71  double mb_angles[MB::CLUSTERS][MB::CRYSTALS][MB::SEGMENTS][Angle::COUNT];
72  LoadMBAngles(mb_angles_file, mb_angles);
73
74  // Initiate event objects.
75  // `TChain::SetBranchAddress` seems to explode if Miniball and/or FAD are not
76  // on the heap - go figure.
77  std::vector<Germanium> *Miniball = new std::vector<Germanium>;
78  std::vector<Annular> *FAD = new std::vector<Annular>;
79  long long EbisTime;
80  long long T1Time;
81  // Additional available structures: SuperCycleTime, ForwardBarrel,
82  // BackwardBarrel, ForwardCD, BackwardCD.
83
84  in_chain.SetBranchAddress("Miniball", &Miniball);
85  in_chain.SetBranchAddress("ForwardCD", &FAD);
86  in_chain.SetBranchAddress("EbisTime", &EbisTime);
87  in_chain.SetBranchAddress("T1Time", &T1Time);
88
89  // Open output file and set up output ROOT structure.
90  TFile output_fh(output_file, "recreate");
91  if (output_fh.IsZombie()) {
92      return ExitStatus::ZOMBIE;
93  }
94  TTree out_tree("is430", "is430");
95
96  int64_t event_id;
97  int64_t ebis_t;
98  int64_t t1_t;
99  // See <http://root.cern.ch/root/html/TTree.html> for "/" syntax.
100  out_tree.Branch("id", &event_id, "id/L");
101  out_tree.Branch("ebis_t", &ebis_t, "ebis_t/L");
102  out_tree.Branch("t1_t", &t1_t, "t1_t/L");
103
104  // Miniball related variables.
105  float ge_e;
106  int64_t ge_t;
107  int ge_clu_id;
108  int ge_cry_id;
109  int ge_seg_id;
110  float ge_theta;
111  float ge_phi;
112  out_tree.Branch("ge_e", &ge_e, "ge_e/F");
113  out_tree.Branch("ge_t", &ge_t, "ge_t/L");
114  out_tree.Branch("ge_clu_id", &ge_clu_id, "clu_id/I");
115  out_tree.Branch("ge_cry_id", &ge_cry_id, "cry_id/I");

```

```

116 out_tree.Branch("ge_seg_id", &ge_seg_id, "seg_id/I");
117 out_tree.Branch("ge_theta", &ge_theta, "ge_theta/F");
118 out_tree.Branch("ge_phi", &ge_phi, "ge_phi/F");
119
120 // Forward AD related variables.
121 float fad_pad_e;
122 float fad_ring_e;
123 float fad_strip_e;
124 int64_t fad_t;
125 int fad_sector_id;
126 int fad_ring_number;
127 int fad_strip_number;
128 float fad_theta;
129 float fad_phi;
130 out_tree.Branch("fad_pad_e", &fad_pad_e, "fad_pad_e/F");
131 out_tree.Branch("fad_ring_e", &fad_ring_e, "fad_ring_e/F");
132 out_tree.Branch("fad_strip_e", &fad_strip_e, "fad_strip_e/F");
133 out_tree.Branch("fad_t", &fad_t, "fad_t/L");
134 out_tree.Branch("fad_sector_id", &fad_sector_id, "fad_sector_id/I");
135 out_tree.Branch("fad_ring_number", &fad_ring_number, "fad_ring_number/I");
136 out_tree.Branch("fad_strip_number", &fad_strip_number, "fad_strip_number/I");
137 out_tree.Branch("fad_theta", &fad_theta, "fad_theta/F");
138 out_tree.Branch("fad_phi", &fad_phi, "fad_phi/F");
139
140 // Loop over events.
141 int64_t nentries = in_chain.GetEntries();
142 int nbytes = 0;
143
144 for (int64_t i = 0; nentries > i; ++i) {
145     int status = EventErrorHandler(in_chain, i);
146     nbytes += status;
147
148     event_id = i;
149     // EBIS window start/ns.
150     ebis_t = EbisTime * EXP::TSTAMP_TO_NS;
151     // ISOLDE proton impact/ns.
152     t1_t = T1Time * EXP::TSTAMP_TO_NS;
153
154     size_t fad_events = FAD->size();
155     for (size_t m = 0; fad_events > m; ++m) {
156         Annular *fad_event = &(*FAD)[m];
157
158         // The ring/strip logic is modelled on known working code from
159         // `CD_histos`.
160         size_t ring_events = fad_event->GetRingNr().size();
161         for (size_t n = 0; ring_events > n; ++n) {
162             // If we have ring event multiplicity two and the next event has the
163             // same ring number, add the energies.
164             if (2 == ring_events &&
165                 fad_event->GetRingNr()[0] == fad_event->GetRingNr()[1]) {
166                 fad_ring_e = fad_event->GetRingEnergy()[0] +
167                     fad_event->GetRingEnergy()[1];
168                 ++n;
169             } else {
170                 fad_ring_e = fad_event->GetRingEnergy()[0];

```

```

171     }
172     fad_ring_number = fad_event->GetRingNr()[0];
173
174     size_t strip_events = fad_event->GetStripNr().size();
175     for (size_t o = 0; strip_events > o; ++o) {
176         // If we have strip event multiplicity two and the next event has the
177         // same ring number, add the energies.
178         if (2 == strip_events &&
179             fad_event->GetStripNr()[0] == fad_event->GetStripNr()[1]) {
180             fad_strip_e = fad_event->GetStripEnergy()[0] +
181                 fad_event->GetStripEnergy()[1];
182             ++o;
183         } else {
184             fad_strip_e = fad_event->GetStripEnergy()[0];
185         }
186         fad_strip_number = fad_event->GetStripNr()[0];
187
188         if (!FADEnergySignalConstraintTrue(fad_ring_e, fad_strip_e)) {
189             // The PSD event is not considered legit; skip.
190             continue;
191         }
192
193         fad_sector_id = fad_event->GetID();
194         FADAngles(fad_sector_id, fad_ring_number, fad_strip_number,
195                 fad_theta, fad_phi);
196
197         fad_pad_e = fad_event->GetEdet();
198         fad_strip_e = fad_event->GetStripEnergy()[0];
199
200         fad_t = EXP::TSTAMP_TO_NS * fad_event->GetTime();
201
202         // Multiplicity of clusters reporting energy signals in the event.
203         size_t mb_cluster_events = Miniball->size();
204         for (size_t j = 0; mb_cluster_events > j; ++j) {
205             Germanium *mb_event = &(*Miniball)[j];
206             // Multiplicity of crystals reporting energy signals in the event.
207             size_t mb_crystal_events = mb_event->GetCrystal().size();
208             for (size_t k = 0; mb_crystal_events > k; ++k) {
209                 // Multiplicity of segments reporting energy signals in the event.
210                 size_t mb_segment_events = mb_event->GetCrystal()[k].GetSeg().size();
211                 for (size_t l = 0; mb_segment_events > l; ++l) {
212                     // An electron will only run ~mm in the detector, so we do not
213                     // need to sum over segments as with photons to catch
214                     // scattering events. In fact, if we do that, we discard true
215                     // events in coincidence with background, and register
216                     // background events from multiple signals.
217
218                     // Energy/keV
219                     float mb_segment_e = mb_event->GetCrystal()[k].GetSeg()[l];
220
221                     if (!Is72GeNeutron(mb_segment_e)) {
222                         continue;
223                     }
224
225                     ge_e = mb_segment_e;

```

```

226
227 // Event time/ns.
228 ge_t = EXP::TSTAMP_TO_NS * mb_event->GetCrystal()[k].GetTime();
229
230 ge_clu_id = mb_event->GetCluID();
231 ge_cry_id = mb_event->GetCrystal()[k].GetCryID();
232 ge_seg_id = mb_event->GetCrystal()[k].GetSegID()[1];
233
234 ge_theta = mb_angles[ge_clu_id][ge_cry_id][ge_seg_id][Angle::THETA];
235 ge_phi = mb_angles[ge_clu_id][ge_cry_id][ge_seg_id][Angle::PHI];
236
237 // Register hit.
238 out_tree.Fill();
239     }
240     }
241     }
242     }
243     }
244     }
245
246 // Progress counter on STDOUT.
247 if (0 == i % 1000) {
248     cout << std::setw(5) << std::setiosflags(ios::fixed) <<
249         std::setprecision(1) << (100.*i)/nentries << " \% done\r" << flush;
250 }
251 }
252 delete Miniball;
253 delete FAD;
254
255 output_fh.Write();
256 output_fh.Close();
257
258 return EXIT_SUCCESS;
259 }

```

```

1  /**
2  * LibNeutrons.hh
3  *
4  * Common utility functions to use when generating intermediate ROOT trees.
5  * Also defines some configuration constants valid for experiment IS430.
6  */
7
8  #ifndef LIBNEUTRONS_H
9  #define LIBNEUTRONS_H
10
11 namespace EventStatus {
12     enum {
13         ERROR = -1,
14         NON_EXISTENT = 0,
15     };
16 };
17
18 namespace ExitStatus {
19     enum {
20         IO_MISSING = 1,

```

```

21     NO_CALTR = 3,
22     ZOMBIE = 4,
23     COULD_NOT_READ_ENTRY = 5,
24     EVENT_NON_EXISTENT = 6,
25     UNEXPECTED_STATUS = 7
26 };
27 };
28
29 namespace Angle {
30     enum {
31         THETA,
32         PHI,
33         COUNT
34     };
35 };
36
37 // Miniball characteristics.
38 namespace MB {
39     const int CLUSTERS = 8;
40     const int CRYSTALS = 3;
41     const int SEGMENTS = 6;
42 }
43
44 namespace EXP {
45     // Convert experiment time quanta to nanoseconds.
46     const int TSTAMP_TO_NS = 25;
47 }
48
49 class TChain;
50
51 int EventErrorHandler(TChain &, int);
52 bool Is72GeNeutron(double);
53 bool FADEnergySignalConstraintTrue(float, float);
54 void FADAngles(int, int, int, float &, float &);
55 void LoadMBAngles(const char *,
56     double [MB::CLUSTERS][MB::CRYSTALS][MB::SEGMENTS][Angle::COUNT]);
57
58 #endif

```

```

1  /**
2   * LibNeutrons.cc
3   *
4   * Common utility functions to use when generating intermediate ROOT trees.
5   */
6
7  #define _USE_MATH_DEFINES
8  #include <cmath>
9  #include <cstdlib>
10 #include <iostream>
11
12 #include <TChain.h>
13 #include <TEnv.h>
14 #include <TFile.h>
15 #include <TRandom.h>
16

```

```

17 #include "CommandLineInterface.hh"
18 #include "LibNeutrons.hh"
19
20 using std::cerr;
21 using std::endl;
22
23
24 /**
25  * Error handling for accessing an event.
26  */
27 int EventErrorHandler(TChain &tchain, const int i)
28 {
29     int status = tchain.GetEvent(i);
30     switch (status) {
31         case EventStatus::ERROR:
32             cerr << "Error occured, could not read entry " << i << " from tree " <<
33                 tchain.GetName() << " in file " << tchain.GetFile()->GetName() << endl;
34             return ExitStatus::COULD_NOT_READ_ENTRY;
35         case EventStatus::NON_EXISTENT:
36             cerr << "Error occured, entry " << i << " in tree " << tchain.GetName() <<
37                 " in file " << tchain.GetFile()->GetName() << " non-existent" << endl;
38             return ExitStatus::EVENT_NON_EXISTENT;
39     }
40     return status;
41 }
42
43
44 /**
45  * Return true if the given event energy is deemed to be neutron-like.
46  */
47 bool Is72GeNeutron(const double gamma_energy_kev)
48 {
49     // 72Ge neutron excitation energy: 690 keV (registered signals including
50     // nucleus recoil closer to ~691 keV).
51     const int ENERGY_WINDOW_KEV_LOWER = 691;
52     const int ENERGY_WINDOW_KEV_UPPER = 721;
53
54     return (ENERGY_WINDOW_KEV_LOWER <= gamma_energy_kev &&
55             ENERGY_WINDOW_KEV_UPPER >= gamma_energy_kev);
56 }
57
58
59 /**
60  * Pick "true" events where strip and ring agree on the energy with at most a
61  * small error.
62  */
63 bool FADEnergySignalConstraintTrue(const float ring_energy,
64     const float strip_energy)
65 {
66     const int MAX_DELTA_RING_STRIP_ENERGY = 500; // keV
67     return (MAX_DELTA_RING_STRIP_ENERGY > std::abs(ring_energy - strip_energy));
68 }
69
70
71 /**

```

```

72  * Find theta and phi angles through laboratory transformations.
73  *
74  * See Johansen, section 5.2.
75  *
76  * See e.g. 'CD_histos.cc' for an implementation of x and y corrections for a
77  * non-orthogonal beam direction.
78  */
79  void FADAngles(const int fad_sector_id, const int ring_number,
80               const int strip_number, float &theta, float &phi)
81  {
82      // Radial distance from AD center.
83      float r = 9. + (gRandom->Rndm() + ring_number) * 2.;
84      // Distance from target.
85      float z = 63.;
86      // Interpret above as cylindrical coordinates that are transformed into
87      // corresponding spherical coordinates; Johansen eq 5.4,
88      // <https://en.wikipedia.org/wiki/Spherical\_coordinates#Cylindrical\_coordinates>
89      theta = atan(r/z);
90
91      // Transformation from Johansen eq 5.5.
92      // M_PI constants defined in 'math.h' dragged in by 'cmath'. M_PI_2 == M_PI/2
93      phi = -.0593411*((float)strip_number + gRandom->Rndm()) + .71209 +
94           M_PI_2*(1-fad_sector_id);
95
96      if (phi > M_PI) {
97          phi -= M_PI;
98      } else if (phi < -M_PI) {
99          phi += M_PI;
100     }
101 }
102
103
104 /**
105  * Load angular mappings for the Miniball segments from the calibration file.
106  */
107 void LoadMBAngles(const char * const file_name,
108                 double mb_angles[MB::CLUSTERS][MB::CRYSTALS][MB::SEGMENTS][Angle::COUNT])
109 {
110     TEnv angles(file_name);
111     for (size_t clu_id = 0; MB::CLUSTERS > clu_id; ++clu_id) {
112         for (size_t cry_id = 0; MB::CRYSTALS > cry_id; ++cry_id) {
113             for (size_t seg_id = 0; MB::SEGMENTS > seg_id; ++seg_id) {
114                 mb_angles[clu_id][cry_id][seg_id][Angle::THETA] = angles.GetValue(Form(
115                     "Theta.%d.%d.%d", clu_id, cry_id, seg_id), 0.0);
116                 mb_angles[clu_id][cry_id][seg_id][Angle::PHI] = angles.GetValue(Form(
117                     "Phi.%d.%d.%d", clu_id, cry_id, seg_id), 0.0);
118             }
119         }
120     }
121 }

```

A.1.2 Histogram creation with Python

A Python infrastructure for creating simple scripts capable of generating histograms both for immediate display on-screen and archived output in several different formats was set up. The histogram output stored in native ROOT trees was used to test modifications of histogram parameters without having to regenerate a full histogram set. PDF output was the main inspection method, which was also used for presenting intermediate results at group meetings. The CSV output (which is not a natively available output format in ROOT) was used as a data export function to be able to render plots in this thesis using the PGFPlots package* in L^AT_EX, with advantages in graphical uniformity within the document and having the entire PGF/TikZ[†] framework easily accessible.

The PyROOT module is more or less feature-complete in its ROOT bindings, though it presents a rather “mechanical” translation of the C++ function calls and as such does not adhere to common Python idioms, nor uses expected native Python data structures where applicable. It also uses the global namespace in non-trivial and initially unexpected ways compared to generic Python modules. There exists another project with the aim of mending such inconsistencies, which, in the tradition of confusing naming schemes, is called ROOTPY.[‡] It was not investigated further for this project.

Since the “heavy lifting”, i.e. the tight and computationally expensive loops, is performed within the external ROOT calls in my use cases, there are no noticeable performance penalties from using a scripted language such as Python. The benefits lie in quick prototyping, and in my personal case also being able to leverage previous Python experience.

There is currently no Python 3 support for PyROOT, so the scripts are written with Python 2.7 in mind.

Select portions of the code are included below, beginning with a script to create the data for forward versus backward angles as seen in e.g. Figure 4.3, and continuing with parts of the utility module code written for the task.

```

----- ge_e_forward_vs_backward.py -----
1  #!/usr/bin/env python
2  # -*- encoding: utf-8 -*-
3  from ROOT import TCanvas
4  from ROOT import TFile
5  from ROOT import TH1F
6  from ROOT import THStack
7
8  import is430_common as is430
9  import root_common as rc
10
11
12  def ge_e_forward_vs_backward():
13      """
14      Draw gamma energies in the energy span around the neutron induced 0+ state
15      in 72Ge from dPE runs for forward and backward detectors respectively with
16      reference to beam impact.

```

*<http://pgfplots.sourceforge.net/>

†<http://sourceforge.net/projects/pgf>

‡<http://www.rootpy.org/>

```

17 """
18 rc.ui.init()
19
20 plot_title = 'Forward and backward #gamma energies.'
21 x_title = 'Energy/keV'
22 y_title = 'Counts'
23 xbins = is430.xbins
24 e_min = is430.e_min
25 e_max = is430.e_max
26
27 f_dPE = TFile(is430.f_all_dpe)
28 t_dPE = f_dPE.Get('is430')
29
30 projections = tuple(
31     {'id': i, 'title': j, 'cut': k} for (i, j, k) in [
32         ('forward', 'Forward detectors (#theta #leq #pi/2)',
33          'ge_theta <= pi/2'),
34         ('backward', 'Backward detectors (#theta > #pi/2)',
35          'ge_theta > pi/2')
36     ]
37 )
38
39 canvas = TCanvas('c_ge_e_forward_and_backward')
40
41 hist_stack = THStack('hs', '{};{};{}'.format(plot_title, x_title, y_title))
42
43 def build_histogram(line_color, projection):
44     print('Processing "{}"...'.format(projection['title']))
45
46     h_name = 'h_{}'.format(projection['id'])
47     h_title = projection['title']
48     h_data = 'ge_e'
49     h_cut = projection['cut']
50
51     histogram = TH1F(h_name, h_title, xbins, e_min, e_max)
52     t_dPE.Project(h_name, h_data, h_cut)
53     # Line color '0' is white, which is less than helpful.
54     histogram.SetLineColor(line_color+1)
55
56     hist_stack.Add(histogram)
57     hist_stack.Draw('nostack')
58     canvas.Update()
59     return histogram
60
61 histograms = [build_histogram(lc, p) for lc, p in enumerate(projections)]
62
63 # Move "Counts" outwards to not clash with the numbers.
64 hist_stack.GetYaxis().SetTitleOffset(1.4)
65
66 canvas.BuildLegend(.5, .9, .9, .8)
67
68 canvas.Update()
69
70 if rc.ui.is_batch_run:
71     is430.batch_output(canvas, histograms, hist_stack)

```

```

72
73     rc.ui.exit()
74
75
76 def main():
77     if rc.ui.is_batch_run:
78         print('Batch run.')
79
80     ge_e_forward_vs_backward()
81
82
83 if __name__ == '__main__':
84     main()

```

```

is430_common/batch_output.py
1  #!/usr/bin/env python
2  # -*- encoding: utf-8 -*-
3  import os
4  import sys
5
6  from ROOT import TFile
7
8  import root_common as rc
9
10
11 def ext_path(extension, title=None):
12     """Return consistent path for output files."""
13     ext_dir = extension
14     prefix = os.path.basename(os.path.splitext(sys.argv[0])[0])
15
16     if title is None:
17         file_name = '{}.{}'.format(prefix, extension)
18     else:
19         file_name = '{}-{}.{}'.format(prefix, title, extension)
20
21     return os.path.join(ext_dir, file_name)
22
23
24 def batch_output(canvas, histograms=None, hist_stack=None):
25     """Write persistent histogram output in PDF, CSV and ROOT format."""
26     canvas_name = canvas.GetName()
27
28     # PDF output
29     canvas.Print(ext_path('pdf', canvas_name))
30
31     # CSV output
32     for histogram in histograms:
33         histogram_name = histogram.GetName()
34         # Sadly the best way I have found to decide if a histogram is 2D or 1D,
35         # since ROOT took the marvellous design decision to make a 1D histogram
36         # a "special case" of a 2D one, so it supports all the same methods,
37         # but with trivial returns. Direct type checking against the base
38         # classes would be another possibility.
39         f = rc.th1f_to_csv if histogram.GetNbinsY() == 1 else rc.th2f_to_csv
40         f(histogram, ext_path('csv', histogram_name))
41

```

```

42     # ROOT file output
43     root_output_file = TFile(ext_path('root', canvas_name), 'recreate')
44     for i in [j for j in histograms + [hist_stack, canvas] if j is not None]:
45         i.Write()
46     root_output_file.Close()

```

```

1  #!/usr/bin/env python
2  # -*- encoding: utf-8 -*-
3  import sys
4
5  from ROOT import gROOT
6  from ROOT import gStyle
7
8
9  is_batch_run = gROOT.IsBatch()
10 is_csv_run = '-csv' in sys.argv
11
12
13 def init():
14     """Initialize sane ROOT environment."""
15     gROOT.Reset()
16     gROOT.SetStyle('Plain')
17     gStyle.SetOptStat(False)
18
19
20 def exit():
21     """Hold canvases open unless we are in batch mode."""
22     if not is_batch_run:
23         raw_input('Press <Enter> to exit')

```

```

1  #!/usr/bin/env python
2  # -*- encoding: utf-8 -*-
3  import csv
4
5
6  def th2f_to_csv(hist, csv_file):
7     """Print TH2F bin data to CSV file."""
8     xbins = hist.GetNbinsX()
9     ybins = hist.GetNbinsY()
10    xaxis = hist.GetXaxis()
11    yaxis = hist.GetYaxis()
12    with open(csv_file, 'w') as f:
13        c = csv.writer(f, delimiter=' ', lineterminator='\n')
14        # Loop over 'y' first, then 'x', to generate output that PGFPlots
15        # handles a lot more efficiently. See section 7.2.1 regarding Matlab
16        # plotting in the PGFPlots manual.
17        #
18        # Discard underflow (bin 0) and overflow (bin 'ybins'+2) from the plot,
19        # but include the overflow bin in the output data since the PGFPlots
20        # routine will discard the last row anyway. It could be a problem if
21        # the overflow value was the minimum or maximum value in the plot,
22        # since the color bar would be skewed accordingly. Most likely it will
23        # always just be zero, though.
24        for ybin in xrange(1, ybins+2):

```

```

25         # Want lower edge of bin and not the center when using the
26         # TH2F-style PGFPlots routine.
27         y_lowedge = yaxis.GetBinLowEdge(ybin)
28         for xbin in xrange(1, xbins+2):
29             x_lowedge = xaxis.GetBinLowEdge(xbin)
30             weight = hist.GetBinContent(xbin, ybin)
31             c.writerow((x_lowedge, y_lowedge, weight))

```

A.1.3 Kinematic curve with MATLAB

To add to the mix of programming languages, minor tasks were occasionally done in MATLAB. Listed below is the script that generated the kinematic curve in Figure 4.13 via Equation (2.7).

```

----- kinematics.m -----
1  MeV_per_u = 931.494061; % MeV/u scale factor.
2
3  % Masses in MeV/c2 from Wolfram Alpha.
4  m_11Be = 11.021657749 * MeV_per_u;
5  m_12B = 12.014352104 * MeV_per_u;
6  m_d = 1876;
7  m_n = 939.56536;
8
9  % Transfer reaction: X(a, b)Y
10 mX = m_d;
11 ma = m_11Be;
12 mb = m_n;
13 mY = m_12B;
14 Ta = 31.35; % E_beam, MeV
15
16 excitation = 0; % Negligible at the studied Ta energies anyway.
17
18 Q = mX + ma - (mb + mY + excitation)
19
20 % The energy-angle relationship exhibits a double-valued behaviour depending on
21 % the sign beneath the square root. In this code this is handled by calculating
22 % each branch until the complex limit and the merging the results.
23 TY_prototype = @(sign) @(theta) ...
24     ( ...
25         ( ...
26             sqrt(ma*mY*Ta).*cos(theta) + ...
27             sign * sqrt( ...
28                 ma*mY*Ta.*cos(theta).^2 + (mY+mb)*(mb*Q + (mb-ma)*Ta)) ...
29             ) ./ (mY+mb) ...
30         ).^2;
31
32 % The real/complex angular limit is analytically given by inspecting the root.
33 real_angular_limit = acos(sqrt(-(mY+mb)*(mb*Q+(mb-ma)*Ta)/(ma*mY*Ta)))
34
35 TY_plus = TY_prototype(+1);
36 TY_minus = TY_prototype(-1);
37
38 theta = [0, real_angular_limit];

```

```
39
40 fplot(TY_plus, theta)
41 hold on
42 fplot(TY_minus, theta)
43 xlabel('\theta / rad')
44 xlim([0, 1])
45 ylabel('T_Y / MeV')
46
47 range = linspace(0, real_angular_limit, 500);
48 out_branch_plus = [range' TY_plus(range)'];
49 out_branch_minus = [range' TY_minus(range)'];
50
51 csvwrite(strcat('dn_ION_', num2str(excitation*1e3), '_plus.csv'), out_branch_plus)
52 csvwrite(strcat('dn_ION_', num2str(excitation*1e3), '_minus.csv'), out_branch_minus)
```